49th AIAA Aerospace Sciences Meeting including the New Horizons Forum and Aerospace Exposition
4 - 7 January 2011, Orlando, Florida

AIAA 2011-649

Direct Numerical Simulations of Turbulent Flow Interactions with Strong Shocks Using Shock-Fitting Method

Pradeep S. Rawat[1] and Xiaolin Zhong[2]
University of California, Los Angeles, CA, 90095

Canonical problem of interaction of a normal shock and isotropic turbulence is fundamental to many important scientific and engineering applications. Most widely used shock capturing methods for the numerical simulation of compressible flows are inherently dissipative, only first order accurate and may incur numerical oscillations near the shock waves. Since high order methods are critical for direct numerical simulation of turbulent flows, we use a shock-fitting method that has been shown to be fifth-order accurate near as well as away from the shock. Moreover, unlike shock-capturing schemes, there are no spurious oscillations even with very strong shock waves. We carry out Direct Numerical Simulation (DNS) of canonical shock-turbulence interaction problem for flows with mean Mach numbers ranging from 2 to 20 and turbulent Mach number varying from 0.12 to 0.38. A Reynolds number based on Taylor microscale, Re_λ, of up to 40 is used, requiring more than 30 million grid points per simulation. Such high mean Mach number values have never been considered in past for study of shock turbulence interactions. Some new trends are observed in turbulent statistics as mean Mach number is increased. Maximum value of streamwise velocity fluctuations downstream of the shock is found to be initially decreasing as Mach number is increased but for stronger than Mach 8 shocks this trend reverses. Similarly maximum streamwise vorticity fluctuations in post-shock flow first increase and then decrease as mean Mach number is increased. We observe that vorticity fluctuations return to isotropy behind the shock for some cases. Increasing mean Mach number and Reynolds number leads to delay in the return to isotropy in the vorticity fluctuations. Overall, the results generally confirm the findings by earlier numerical simulations and provide new trends for stronger shocks than those considered by numerical studies in the past.

1 INTRODUCTION

Many important scientific and engineering applications involve complex interactions between turbulent flows and strong shocks. Very high rates of compression and expansion waves in turbulent flows are observed in a number of explosive phenomena such as volcanic eruptions, detonations, shock wave lithotripsy to break up kidney stones, supernova explosion, as well as the implosion of a cryogenic fuel capsule for inertial confinement fusion (ICF). These processes are strongly nonlinear and proven to be very complex to understand with existing tools. The problem of interaction of the turbulence and normal shock is fundamental for better understanding of such complex phenomena. The relevant problem for the present study is interaction of normal shocks with free turbulence as shown in Fig. 1. Complex linear and non-linear mechanisms are involved in this problem that significantly affect the shock wave as well as the turbulence statistics. This fundamental shock-turbulence interaction problem has been a challenge for experimentalists, theorists and computational researchers for more than fifty years.

---

[1] Graduate Student, Mechanical and Aerospace Engineering Deptt. pradeep@seas.ucla.edu, Student Member, AIAA
[2] Professor, Mechanical and Aerospace Engineering Department, Associate Fellow, AIAA.

Numerical simulation of such complex problems warrants very high-order numerical methods. High-order shock capturing schemes have been the methods of choice in most previous numerical simulation studies of shock turbulence interaction[1-4]. However, popular shock-capturing schemes reduce to first order accuracy near the shock due to the use of dissipation near the shock [5-7]. Moreover, spurious numerical oscillations have been observed when solving strong-shock and turbulence interaction problems with shock-capturing schemes[7, 8]. In our previous work [6, 9, 10], we presented shock-fitting algorithms that converge with high-order accuracy near as well as away from the shock. These methods were also extended for direct numerical simulation of shock-turbulence interactions [10]. In this paper, we present extensive results to estimate effects of mean Mach number, turbulent Mach number and Reynolds number on post-shock flow in shock-turbulence interactions. A brief summary of the literature in the field is presented in ensuing sections followed by the scope of current study.

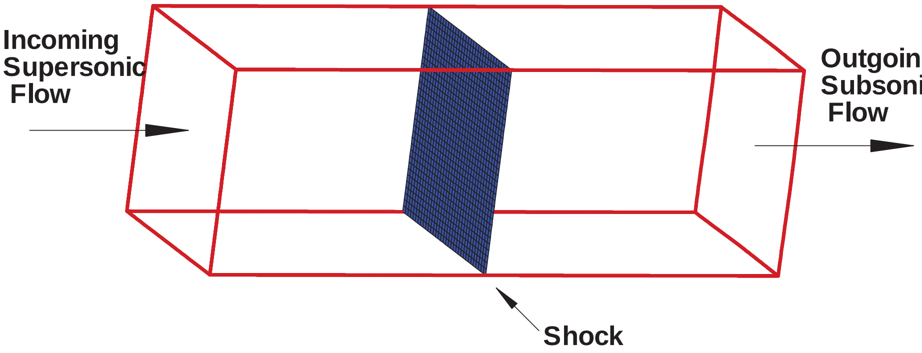

Fig. 1: A schematic of typical setting of isotropic shock and turbulence interaction.

1.1 Theoretical Studies

Theoretical studies in this field have been attempted mostly through linear interaction analysis, where small perturbations in flow are considered. Kovasznay [11] showed that weak turbulent fluctuations of velocity, pressure and entropy about mean uniform flow can be decomposed into vorticity, acoustic and entropy modes. Each of these modes were shown to evolve independently for the first order approximation under inviscid flow assumption for mean uniform flow. Ribner [12-14] and Moore [15] were among the earliest researchers to carry out theoretical shock-turbulence interaction analysis. Ribner [12] analyzed interaction of a plane sinusoidal disturbance in velocity passing through a shock as a boundary value problem. In his analysis the shock was kept steady by solving the equations in a moving reference frame. It was found that initial velocity wave is amplified and refracted by the shock. He later generalized this result from single wave to obtain shock-interaction effects of a completely turbulent velocity field [13] and obtained significant turbulent amplification due to shock turbulence interaction. Moore [15] performed unsteady analysis of interaction of obliquely traveling weak plane disturbances of arbitrary profile with a plane normal shock. Unlike Ribner's analysis, unsteady shock was considered for linear analysis the interaction of sound and vorticity waves with an unsteady shock. It was found that amplification of disturbances depends on impingement angle and Mach number of the shock. McKenzie and Westphal [16] derived formulas for amplification and Snell's Laws for refraction and reflection of acoustic, vorticity and entropy waves interacting with shock and applied the results to the amplification of small disturbances in the solar wind on a passage through the bow shock of earth. More recent theoretical studies of shock and turbulence interaction are by Goldstein [17], Lee et al. [1, 18, 19], Mahesh et al. [2, 3, 20] and Fabre et al. [21, 22]. It was found in these studies that different components of the turbulent kinetic energy, as well as fluctuations in pressure, temperature and density are amplified across the shocks. Despite several assumptions, Linear Interaction Analysis (LIA) satisfactorily predict essential characteristics of the interaction.

1.2 Numerical Studies

Since the early 80s, various attempts have been made towards the numerical simulation of shock and turbulence interaction. Initial efforts in this regard considered interaction of the shock with simple waves. In 1981, Pao and Salas [23] fitted the shock at inflow boundary and solved Euler equation with finite difference discretization for study of shock/vortex interaction. Shock fitting computations with pseudo-spectral (Zang et. al [24]) and spectral techniques (Hussaini et al [25, 26]) were later used to treat the problems in which a single vortex, a vortex sheet, an entropy spot or acoustic wave interacts with the shock. The results obtained from these numerical efforts confirmed the linear theory in the regime of weak shocks. With the advent of essentially non-oscillatory (ENO) and related schemes, shock-capturing methods gained popularity for simulations of compressible flows. A number of new schemes for compressible flows has since been tested for interaction of shock with small disturbances against the results obtained from linear theory [26-28]. Although limited to low Mach numbers, these studies mostly confirm the LIA results.

The numerical studies of fully turbulent field interacting with shocks are more recent. For the simulation of the turbulent field DNS methods and large eddy simulations (LES) have been used. However these different types of methods give different results when interaction with shock is considered [29]. Most of the recent direct numerical simulation (DNS) studies have been on various aspects of interaction of a normal shock with freestream turbulence for relatively weak shocks of small Mach numbers. For example, Mahesh et al. [2, 3] did extensive direct numerical simulation (DNS) study of the interaction of a normal shock with an isotropic turbulence. The mean shock Mach numbers were in the range of 1.29 to 1.8. They found that the upstream correlation between the vorticity and entropy fluctuations has strong influence on the evolution of the turbulence across the shock. They also used linear analysis to analyze the simulation results. Other shock/turbulence interaction studies have been conducted by the same group of workers [18, 30]. Lee et al. [18] investigated the effect of Mach number on isotropic vertical turbulence interacting with a shock wave. The range of Mach numbers was in the range from 1.5 to 3.0. A shock-capturing scheme was developed to accurately simulate the unsteady interaction of turbulence with shock waves. It was found that turbulence kinetic energy is amplified across the shock wave, and this amplification tends to saturate beyond Mach 3. Hannapel et al. [31] computed interaction of a Mach 2 shock with a third order in space shock-capturing scheme based on the essentially non-oscillatory ENO algorithm of Harten together with an approximate Riemann solver. Jamme et al. [4] carried out a Direct Numerical Simulation (DNS) to study the interaction between normal shock waves of moderate strength (Mach 1.2 and Mach 1.5) and isotropic turbulence. Adams and Shariff [32, 33] proposed a class of upwind-biased finite-difference schemes with a compact stencil for shock/turbulence interaction simulation. They used this nonconservative upwind scheme in smooth region while a shock-capturing ENO scheme was turned on around discontinuities. This idea of hybrid formulation was improved by Pirozzoli [34] who used similar hybrid formulation for a compact weighted essentially non-oscillatory (WENO) scheme with conservative formulation for the simulation of shock turbulence interaction. Ducros et al. [35] developed larger-eddy simulation(LES) on the shock/turbulence interaction by using a second-order finite volume scheme. The method was then used to simulate the interaction of a Mach 1.2 shock with homogeneous turbulence.

Recently, there has been more focus towards the strong shock and turbulence interactions. Larsson et al.[36] considered shock-turbulence interaction problem with a hybrid scheme which uses flow paramters based sensor to switch between high order WENO scheme and a high order central difference scheme. They investigated shock waves as strong as Mach 6 shocks and carried out highly resolved simulations. They observed that vorticity fluctuations return to isotropy behind the shock. Grube et al.[37] used 4th order bandwidth-optimized WENO schemes to compute interaction of highly compressible turbulence with a Mach 5 shock. They reported results of turbulence statistics being similar to the case of weakly compressible flows but also observed highly distorted shock shapes in some instances.

It is observed that most of the studies in field of shock-turbulence interaction used shock capturing and did not go beyond computations of Mach 3 shocks. The reason for that could be decrease in shock thickness as shock gets stronger since shock-capturing schemes will need a finer resolution for that case. Recently, Sesterhenn et al. [38] revisited shock-fitting schemes and applied them for solving Navier-Stokes equations in non-conservative form for problem of interaction of Mach 3 shock with isotropic turbulence. Shock-fitting considers the shock as a discontinuity. Hence, unlike shock-capturing schemes, it is not limited by need of finer resolution around the shock and should be easily applicable for DNS studies of strong shocks.

1.3 Shock-Fitting Methods

Shock fitting schemes have been used for simulations of compressible flow with well-defined shocks since 1960s. Moretti and collaborators developed efficient and reliable codes using shock fitting for steady and time-dependent flows [39-42] . In order to compute shock velocities, the Rankine-Hugoniot conditions were used with a compatibility equation along a generator of the characteristic conoid reaching the shock. Later a modification of the scheme was used by de Neef and Moretti [43] where temporal derivatives of the Rankine-Hugoniot conditions were used with characteristic equations to find the shock velocity. Since such flows do not need any shock capturing, conservative forms of the governing equations were not required. Moretti used Reimann's characteristic equations; discretizing them based on the direction of propagation of the associated waves. Such methods were named λ-schemes [44] and were used exclusively with shock-fitting method [45-49]. Moretti also considered multi-dimensional flows where shocks are not aligned with any grid lines but float across the grids [50]. Further work was done on this floating shock-fitting technique to make it simpler [51, 52]. However, topological problems were encountered if more than one shock were present. A review of the development of the shock fitting methods can be found in Refs. [53, 54].

Original shock-fitting schemes with grids aligned with the shock were adopted by a number of researchers. In the 1990's shock-fitting was used mostly for solving flow over blunt bodies. The bow shocks were treated as a computational boundary. Pseudo-spectral approximations to the Euler equations employing shock fitting were first performed by Hussaini et al. [25]. Kopriva [55, 56] used Chebyshev spectral collocation method, in conjunction with shock-fitting and extended it to multidomain [57]. Cai [58] used a shock-fitting algorithm to compute two-dimensional detonation waves. Zhong [59] developed new high-order finite difference schemes and coupled them with shock-fitting algorithm for the study of hypersonic boundary layers. These schemes were used for the receptivity studies for supersonic boundary layers [60-64]. Recently, Brooks and Powers [65] have extended Kopriva's spectral method with shock fitting to solve two-dimensional axisymmetric Euler equations in a cylindrical coordinate frame for blunt body problem.

As discussed earlier, shock-fitting method has also been applied to problem of shock and disturbance interactions. Sesterhenn et al. [22, 38] decomposed inviscid part of the three-dimensional Navier-Stokes equations in characteristic (acoustic and convective) waves aligned with the numerical grid. Variables representing these characteristic waves are discretized using a compact fifth-order upwind scheme. This method is an extension of Moretti's λ-schemes and has been validated for the problems of shock and entropy spot interaction and the shock and isotropic turbulence interaction. This scheme is different from the shock-fitting scheme we are using [59]. We solve the Navier-Stokes equation in conservative form as opposed to the non-conservative formulation used by Sesterhenn et al. [38] since it enables us to capture weak discontinuities behind the main shock.

It has been discussed in literature [38, 66] that smallest length scale η (Kolmogorov length scale) and shock thickeness δ in the compressible flow are related as: $\eta/\delta \approx 0.13\sqrt{\mathrm{Re}_\lambda}\,(M-1)/M_t$. For the stronger shocks and small turbulent Mach numbers shock thickness is actually one to two orders of magnitude lesser than the smallest length scales captured in the simulations. Moreover, the Navier Stokes equations are considered invalid inside the shock. Shock capturing schemes spread the shock artificially over finite number (generally 5-6 grid points). On the other hand, shock fitting algorithm considers the shock a sharp interface and exact jump conditions across the shock are implemented. Hence, results from shock fitting algorithm are expected to approximate the real physics of the problem well for strong shocks. These shock fitting schemes have been widely used in past for highly accurate simulations of hypersonic flows [60, 61, 64, 67]. Shock fitting methods consider the shock as a sharp discontinuity and there is no numerical smearing of the shock fronts. Compared to shock capturing methods, the main advantage of shock fitting methods is the possibility of achieving uniform high-order accuracy for flow containing shock waves and avoiding possible spurious oscillations. On the contrary, most of the popular shock-capturing methods are only first-order accurate at the shock and may incur spurious numerical oscillations near the shock

1.3 Motivation and Scope of Current Study

A study of the literature in the field of shock interactions with turbulence shows that current scientific understanding of shock-turbulence interactions in complex configurations and the ability to reliably predict these strongly nonlinear flows remains limited. Most of the popular methods for solving compressible flow involve shock-capturing algorithms for treatment of shock. However, it has been observed that even high-order shock capturing methods give low accuracy at the shock [5] and might lead to spurious oscillations [8]. Many shock capturing method introduce some dissipation to avoid spurious oscillations which, however, is not accurate enough for simulation of turbulent flow. On the other hand, conventional high-order methods generally used for DNS studies have numerical problems due to strong gradients around shock. Thus, DNS of shock and isotropic turbulence interaction has not been possible for stronger than Mach 6 shocks due to limitations of computational resources for the used shock capturing algorithms.

Current work is continuation of our efforts presented in Refs.[6, 9, 10]. Here, underlying idea is to develop and use shock-fitting along with high order schemes to gain knowledge about nonlinear phenomena involving interaction of strong shocks and turbulent flows. Shock fitting algorithms treat the shock interface sharply without any dissipation hence they are compatible with low dissipation schemes used for DNS of turbulent flow. Shock fitting methods are ideally suited for the cases where there is a clearly demarcated interface which is indeed the case for the problem of turbulent flow incoming to a strong shock as shown in Fig. 1. In our previous work [6, 9], some simple canonical problems were considered by us and results obtained point to the high-order accuracy of the shock-fitting methods for such problems.

In our previous work we have developed and evaluated the shock-fitting methodology for canonical problems where flow disturbances interact with a strong shock [6, 9] in one and two dimensional setups. It was observed that results from shock-fitting methods for such problems showed uniformly high-order convergence and did not incur any spurious numerical oscillations. On the other hand, the popular shock-capturing methods were found to be only first order with non-physical oscillation around the shock. Since high-order accuracy is desired for the simulation of turbulent flow, shock-fitting methods provide a very good alternative to the shock-capturing method when a well defined strong shock is present in the flow. We extended this method for simulation of shock and turbulence interactions [10]. Focus of the current study is to carry out extensive parametric study of canonical shock turbulence interaction problem using shock-fitting DNS as a tool. Thrust is mainly on strong shocks which have not been considered in past due to computational limitations of the prevalent numerical methods. In remaining part of this paper we briefly present the governing equations and numerical method for shock-fitting algorithm. This is followed by the discussions on shock fitting implementation for shock turbulence interactions and results for shock and turbulence interactions.

2 GOVERNING EQUATIONS

The governing equations are compressible Navier-Stokes equations which are given as follows :

$$\frac{\partial \rho}{\partial t} + \nabla.(\rho \mathbf{u}) = 0 \tag{1}$$

$$\rho\left(\frac{\partial \mathbf{u}}{\partial t} + \mathbf{u}\cdot\nabla\mathbf{u}\right) = -\nabla p + \nabla\cdot\overset{=}{\tau} \tag{2}$$

$$\frac{\partial e}{\partial t} + \nabla\cdot(e\mathbf{u}) = -\nabla\cdot(p\mathbf{u}) + \nabla\cdot(\mathbf{u}\cdot\overset{=}{\tau}) - \nabla\cdot\mathbf{q} \tag{3}$$

where $e = \frac{p}{(\gamma-1)} + \frac{1}{2}\rho U^2$, is the internal energy plus the kinetic energy of the fluid.

All the terms in the above governing equations are in nondimensionalized form where important characteristics of the flow upstream of the shock are used for nondimensionalization. Simulation of incoming isotropic turbulence is carried out as a temporal simulation in a periodic box. Initial conditions for periodic box are random fluctuations in flow variables with prescribed spectra (with k_0 as the most energetic wave number) and given velocity fluctuations. Root mean square (rms) values of these velocity fluctuations u_0^*, upstream fluid density ρ_1^* and temperature T_1^* are chosen to nondimensionalize all the flow variables and functions. Length is nondimenionalized by $k_0\lambda_0^*/2$ where λ_0^* is the Taylor microscale.

The viscous stress and the heat flux are given by the usual constitutive equations in Newtonian fluid as follows

$$\tau_{ij} = \mu\left(\frac{\partial u_i}{\partial x_j} + \frac{\partial u_j}{\partial x_i}\right) - \frac{2}{3}\mu\frac{\partial u_k}{\partial x_k}\delta_{ij} \tag{4}$$

$$q_i = -k\frac{\partial T}{\partial x_i} \tag{5}$$

where μ is the viscosity coefficient determined by the power law,

$$\mu = \mu_0\left(T/T_0\right)^{0.76} \tag{6}$$

where μ_0 and T_0 are reference values. The thermal conductivity k is computed from the Prandtl number, which is assumed constant at 0.7 in this paper.

3 NUMERICAL METHOD

We use a fifth-order shock-fitting algorithm treating the shock as a sharp entity. For the preliminary results presented in this paper, the shock is taken as boundary of the computational domain and fifth-order shock-fitting method of Zhong [59] is used for solving the flow between shock and exit boundary (Fig. 1). The flow variables behind the shock are determined by Rankine-Hugoniot relations across the main shock and a characteristic compatibility relation from behind the shock. The velocity and location of the shock are solved as part of the solutions. In the interior, solution of conservative compressible Navier-Stokes equations is carried out using the numerical method described in this section.

In numerical simulation, the compressible Navier-Stokes equations (2) to (4) are written in the following conservative form,

$$\frac{\partial U}{\partial t} + \frac{\partial E}{\partial x} + \frac{\partial F}{\partial y} + \frac{\partial G}{\partial z} + \frac{\partial E_v}{\partial x} + \frac{\partial F_v}{\partial y} + \frac{\partial G_v}{\partial z} = 0 \tag{7}$$

where U is the solution vector given by

$$U = \{\rho, \rho u, \rho v, \rho w, e\} \tag{8}$$

E, F, G are the inviscid flux terms, and E_v, F_v, G_v are the viscous terms. They are written as follows

$$E = \begin{Bmatrix} \rho u \\ \rho u^2 + p \\ \rho uv \\ \rho uw \\ (e+p)u \end{Bmatrix} \tag{9}$$

$$F = \begin{Bmatrix} \rho v \\ \rho vu \\ \rho v^2 + p \\ \rho vw \\ (e+p)v \end{Bmatrix} \tag{10}$$

$$G = \begin{Bmatrix} \rho w \\ \rho wu \\ \rho wv \\ \rho w^2 + p \\ (e+p)w \end{Bmatrix} \tag{11}$$

$$E_v = \begin{Bmatrix} 0 \\ \tau_{xx} \\ \tau_{yx} \\ \tau_{zx} \\ u\tau_{xx} + v\tau_{yx} + w\tau_{zx} - q_x \end{Bmatrix} \tag{12}$$

$$F_v = \begin{Bmatrix} 0 \\ \tau_{xy} \\ \tau_{yy} \\ \tau_{zy} \\ u\tau_{xy} + v\tau_{yy} + w\tau_{zy} - q_y \end{Bmatrix} \tag{13}$$

$$G_v = \begin{Bmatrix} 0 \\ \tau_{xz} \\ \tau_{yz} \\ \tau_{zz} \\ u\tau_{xz} + v\tau_{yz} + w\tau_{zz} - q_z \end{Bmatrix} \tag{14}$$

In the conservative equation (7), the inviscid fluxes and the viscous fluxes have the same forms as those of the Navier-Stokes equations. Before discretizing the governing equations by a finite difference method, equation (7) in the physical domain is transformed to the shock and boundary fitted computational domain by the following transformation relations,

$$\begin{cases} \xi = \xi(x,y,z) \\ \eta = \eta(x,y,z) \\ \varsigma = \varsigma(x,y,z) \\ \tau = t \end{cases} \Leftrightarrow \begin{cases} x = x(\xi,\eta,\varsigma,\tau) \\ y = y(\xi,\eta,\varsigma,\tau) \\ z = z(\xi,\eta,\varsigma,\tau) \\ t = \tau \end{cases} \tag{15}$$

and the transformed governing equation in the computational domain is expressed as follows

$$\frac{1}{J}\frac{\partial U}{\partial \tau} + \frac{\partial E'}{\partial \xi} + \frac{\partial F'}{\partial \eta} + \frac{\partial G'}{\partial \varsigma} + \frac{\partial E'_v}{\partial \xi} + \frac{\partial F'_v}{\partial \eta} + \frac{\partial G'_v}{\partial \varsigma} + U\frac{\partial\left(\frac{1}{J}\right)}{\partial \tau} = 0 \tag{16}$$

An explicit finite difference scheme is used for spatial discretization of the governing equation (16), the inviscid flux terms are discretized by a fifth-order upwind scheme, and the viscous flux terms are discretized by a sixth-order central scheme. For the inviscid flux vectors, the flux Jacobians contain both positive and negative eigenvalues. A simple local Lax-Friedrichs scheme is used to split vectors into negative and positive wave fields. For example, the flux term F′ in Eq (18) can be split into two terms of pure positive and negative eigenvalues as follows

$$F' = F'_+ + F'_- \tag{17}$$

where $F'_+ = \frac{1}{2}\left(F' + \lambda U\right)$ and $F'_- = \frac{1}{2}\left(F' - \lambda U\right)$ and λ is chosen to be larger than the local maximum eigenvalue of F′.

$$\lambda = \frac{|\nabla \eta|}{J}\left(\sqrt{\left(\varepsilon c\right)^2 + u'^2} + c\right) \tag{18}$$

where

$$u' = \frac{\eta_x u + \eta_y v + \eta_z w + \eta_t}{|\nabla \eta|} \tag{19}$$

The parameter ε is a small positive constant added to adjust the smoothness of the splitting. The fluxes F'_+ and F'_- contain only positive and negative eigenvalues respectively. Therefore, in the spatial discretization of Eq. (7), the derivative of the flux F is split into two terms

$$\frac{\partial F'}{\partial \eta} = \frac{\partial F'_+}{\partial \eta} + \frac{\partial F'_-}{\partial \eta} \tag{20}$$

where the first term on the right hand side is discretized by the upwind scheme and the second term by the downwind scheme.

The fifth-order explicit scheme utilizes a 7-point stencil and has an adjustable parameter α as follows

$$u'_i = \frac{1}{hb_i}\sum_{k=-3}^{3} a_{i+k}u_{i+k} - \frac{\alpha}{6!b_i}h^5\left(\frac{\partial^6 u}{\partial x^6}\right)_i + \ldots \tag{21}$$

where $\alpha_{i\pm3} = \pm1 + \frac{1}{12}\alpha,\ \alpha_{i\pm2} = \mp9 - \frac{1}{2}\alpha,\ \alpha_{i\pm1} = \pm45 + \frac{5}{4}\alpha,\ \alpha_i = -\frac{5}{3}\alpha$ and $b_i = 60$. The scheme is upwind when α < 0 and downwind when α > 0. It becomes a 6-order central scheme when α = 0 which is used for discretizing viscous terms.

4 DNS OF SHOCK-TURBULENCE INTERACTION: IMPLEMENTATION

As shown in Fig. 1, incoming flow to the shock wave is supersonic for the problem under consideration and shock fluctuations are small for the cases considered in this study. Hence, the flow upstream of the shock is not affected by the nominally normal shock wave or the flow downstream. For computational efficiency, supersonic turbulent flow ahead of the shock wave can be computed in separate simulation. Hence, computational domain for the shock fitting method for shock-turbulence interaction problem consists of flow only downstream of the shock. A schematic of the shock-fitting implementation for the shock-turbulence interaction problem is shown in Fig. 2. We first compute decaying isotropic turbulence in a periodic box to generate the realistic turbulent fluctuations that can be used as incoming turbulence for the shock-fitting algorithm. This is shown schematically in Fig. 2(a). Using the Taylor hypothesis, the turbulent fluctuations generated from Fig. 2(a) are imposed on supersonic flow and used as inflow condition at the shock. The computational domain for implementation of shock-fitting algorithm is shown in Fig. 2(b) where the shock front forms the left boundary. Periodic boundary conditions are used in the transverse directions and non-reflecting characteristic boundary conditions are used at the subsonic exit of the computational domain.

Reliable numerical simulation of shock and turbulence interaction needs good approximation to realistic turbulence as the inflow condition. Ideally, one should generate spatially evolving turbulence and prescribe it just behind the shock. Such turbulence should be statistically stationary and homogeneous in transverse directions while evolving in streamwise direction. Obtaining spatially evolving turbulence with desired statistics is expensive since fields for these computations are needed to be computed and averaged over time as well as transverse directions. On the other hand, computation of temporally decaying isotropic turbulence is much simpler and computationally inexpensive as periodic boundary conditions are used and all the statistics are obtained from only one snapshot of the flow field. A common practice [1-4, 36, 37] for providing inflow conditions has been to compute decaying isotropic turbulence and convect the flow field with mean streamwise velocity using Taylor's hypothesis [68] of ``Frozen Turbulence''. Lee et al. [69] investigated validity of Taylor's hypothesis for solenoidal turbulence in compressible flows and found that spatially evolving turbulent statistics can be approximated really well by those obtained from a temporal simulation using Taylor's hypothesis if the turbulent fluctuations are small enough. It is recommended to have turbulent Mach number, $M_t < 0.5$, and turbulent intensity, $u_{1rms} / \overline{u}_1 < 0.15$, with solenoidal incoming turbulence for application of Taylor's hypothesis. These requirements align well with the scope and utility of our shock-fitting method. Hence, in this study, we generate the inflow conditions from temporal simulation of initially solenoidal turbulence in a periodic box and use Taylor's hypothesis to convect the turbulent fluctuations with mean flow velocity as inflow condition for shock-fitting computation.

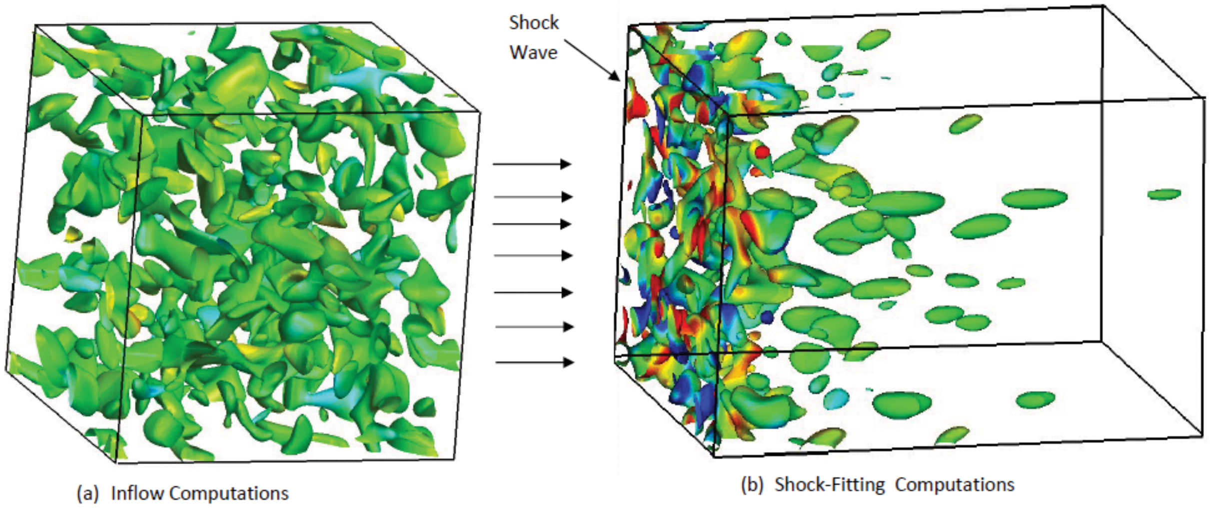

(a) Inflow Computations

(b) Shock-Fitting Computations

Fig. 2: Schematic showing computational domains and typical streamwise vorticity iso-contours (colored by transverse vorticity contours) for simulation of shock-turbulence interaction using shock-fitting algorithm. The inflow turbulence is generated by simulation of decaying isotropic turbulence in a periodic box as shown in (a). The turbulent fluctuations are imposed as left boundary condition of the actual computational domain for shock-fitting algorithm as shown in (b).

4.1 Inflow Computation: Decaying Isotropic Turbulence

Simulation of decaying isotropic turbulence in a periodic box is started with initial conditions generated using the algorithm given by Erlebacher et al [70]. The algorithm is based on generating random fields for fluctuations of flow variables and imposing a given spectrum. Following spectrum is imposed on the fluctuations of flow variables:

$$E(k) \propto k^4 \exp\left[-2\left(k/k_0\right)^2\right] \tag{22}$$

Where $k = \sqrt{k_1^2 + k_2^2 + k_3^2}$ is the wave number of fluctuation and k_0 is the most energetic wave number. This method offers flexibility to generate various turbulent regimes.

The most important parameters that govern the physics of shock turbulence interactions are turbulent Mach number M_t and Reynolds number based on Taylor microscale λ. These quantities are defined as follows:

$$M_t = q/\bar{c} \tag{23}$$

Where,

$$q = \left(\widetilde{u_i'' u_i''}\right)^{\frac{1}{2}} \tag{24}$$

and

$$\mathrm{Re}_\lambda = \bar{\rho} u_{rms} \lambda / \bar{\mu} \tag{25}$$

In this paper, for any given variable f, $\bar{f}$ denotes an ensemble average and $\tilde{f}$ is mass-weighted average i.e. $\tilde{f} = \overline{\rho f}/\bar{\rho}$. Deviation from ensemble average and mass-weighted average is denoted as f' and f'' respectively. Subscript '1' has been used to denote the quantities upstream of the shock. Speed of sound is denoted as c, $u_{rms} = \left(\widetilde{u_1''^2}\right)^{1/2}$ and Taylor microscale is $\lambda = \left(\lambda_1 + \lambda_2 + \lambda_3\right)/3$ where

$$\lambda_\alpha = \left[\overline{u'^2_\alpha} \Big/ \overline{\left(\frac{\partial u'_\alpha}{\partial x_\alpha}\right)^2}\right]^{1/2} \qquad (\alpha = 1,\, 2 \text{ or } 3) \tag{26}$$

With the nondimensionalized governing equations following parameters are used as initial condition for generating initial random fluctuations: upstream mean density, $\rho_1 = 1$, temperature $T_1 = 1$, initial rms value of velocity fluctuations $u^0_{rms} = 1$, $\mathrm{Pr} = 0.7$, $\gamma = 1.4$. Any values of initial turbulent Mach number, M_{t0}, and initial Reynolds number, $\mathrm{Re}_{\lambda 0}$ are can be chosen. Nodimensionalized gas constant is given by $R = 3/\gamma M^2_{t0}$ and reference viscosity is given as $\mu_0 = \rho_1 u^0_{rms} \lambda_0 / \mathrm{Re}_{\lambda,0}$ $\lambda_0 = 2/k_0$.

The initial conditions are assigned in a box of dimension $(2\pi)^3$ and compressible Navier-stokes equations are solved using periodic boundary conditions in all three directions until reasonably realistic turbulence is achieved. We use a fifth order upwind finite-differencing scheme [59] for this purpose. Skewness of streamwise velocity derivatives is an important parameter that is monitored during the simulation of decaying isotropic turbulence. This parameter is defined as follows:

$$S_1 = \overline{\left(\partial u_1' / \partial x_1\right)^3} \Big/ \left[\overline{\left(\partial u_1' / \partial x_1\right)^2}\right]^{3/2} \tag{27}$$

Skewness of velocity derivatives is a measure of inertial non-linearity of turbulence. For the parameters considered here, a realistic turbulence should have S_1 in the range -0.4 to -0.6 [1, 3, 4]. In all of our calculations of inflow turbulence we found that S_1 reaches steady state in $t \sim \lambda_0 / u_{rms}^0$. A representative variation of various statistics obtained from simulations is shown in Fig. 3 for flow with initial parameters $M_{t0} = 0.175$ and $\mathrm{Re}_{\lambda 0} = 135$. These computations were performed with 512^3 grid points. Apart from S_1, we also plot variance of dilatation fluctuations, $d = \partial u_i / \partial x_i$, variance of velocity fluctuations, turbulent Mach number, M_t, and Reynolds number based on Taylor microscale, Re_λ. It can be seen that velocity fluctuations are dissipated with the time, leading to decay in turbulent Mach number as well as Taylor microscale. Sudden increase in dilatation is due to completely solenoidal initial conditions and has been reported in previous studies as well[71, 72].

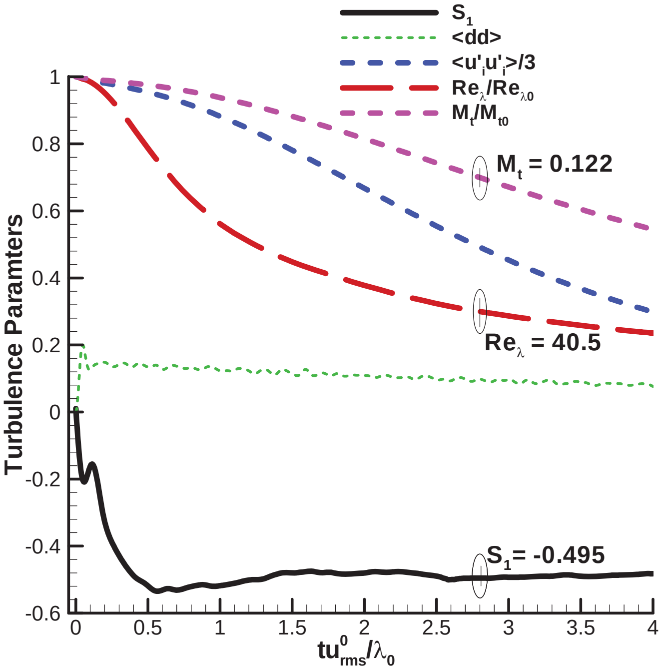

Fig. 3: Evolution of various turbulence statistics in simulation of decaying isotropic turbulence. ($M_{t0} = 0.175$, $\mathrm{Re}_{\lambda 0} = 135$)

After the skewness of velocity derivative, S_1, becomes steady to have value between -0.4 and -0.6, we choose a flow-field with desired values of M_t and Re_λ as inflow condition for the shock-fitting computations. For example, for the case shown in Fig. 3, flow field at $t = 2.8\lambda_0 / u_{rms}^0$ is prescribed upstream of the shock which corresponds to $M_t = 0.122$, $\mathrm{Re}_\lambda = 40.5$ and $S_1 = -0.49$ for the incoming turbulence. One can vary the flow conditions of decaying isotropic turbulence to obtain well developed realistic turbulence with desired statistical properties.

4.2 Shock-fitting implementation

The computational domain for implementation of shock-fitting algorithm is shown in Fig. 2(b). The shock forms the left boundary of the computational domain. The turbulent fluctuations generated from Fig. 2(a) on a periodic box of dimensions $2\pi^3$ are imposed on supersonic flow and used as inflow condition at the shock. For shock-fitting computations we use a domain of size $4\pi \times 2\pi^2$ and same non-dimensionalization is used as used for inflow computations. Periodic boundary conditions are used in the transverse directions and non-reflecting characteristic boundary conditions are used at the subsonic exit of the computational domain.

In the shock-fitting algorithm, the grid distorts with movement of the shock front. Turbulent fluctuations described in the previous section are imposed on corresponding supersonic flow following Taylor's hypothesis that is valid for small turbulent intensities ($M_t < 0.5$ and $u_{1rms} / \overline{u}_1 < 0.15$). For higher turbulent intensities, it is advisable to carry out simulation of spatially decaying turbulence which is more expensive. From the temporal simulations inside a periodic box, we obtain values of flow variables at fixed grid points of the box while due to shock-movement grid points in shock-fitting computations are not stationary. Moreover, when the turbulent box is convected through the shock in the shock-fitting computations, the shock-points generally do not align with grid points of the turbulent box. Hence, values on the supersonic side of the shock are computed using interpolations. Since in our shock-fitting formulation the grids move in only one direction (X-direction in Fig. 2(b)), one dimensional interpolation using Fast Fourier Transform (FFT) is sufficient for this purpose. As a boundary condition, shock-fitting formulation needs the values of the time derivatives of conservative variables ahead of the shock according to the isotropic field which using Taylor's hypothesis are taken as appropriate spatial derivatives. Together with one characteristic coming to the shock from the high pressure side, these values determine the shock velocity. Thus, downstream flow variables are calculated from the corresponding upstream values, using the Rankine–Hugoniot conditions.

Uniform conditions corresponding to laminar Rankine-Hugoniot jump conditions are used as initial condition for simulation of post-shock flow. As the shock interacts with the incoming flow, transients are generated. Several flow-through of inflow box are needed before turbulence statistics in post-shock flow reach a steady state. Periodic boundary conditions are used in the transverse directions and non-reflecting characteristic boundary conditions [73] are used at the subsonic exit of the computational domain. This involves prescribing a back pressure at the exit. Since, the value of the back pressure is not known beforehand, we assign the laminar value of pressure for this purpose. This was found to be sufficient for the low turbulence fluctuations suitable for shock-fitting method. To present the effect of the boundary conditions, we present results from our normal domain of size $4\pi \times 2\pi^2$ and a longer domain $6\pi \times 2\pi^2$ for same inflow in Fig. 4. The presented results are computed with incoming flow having mean Mach Number, $M_1 = 20$, turbulent Mach number, $M_t = 0.275$, and incoming Taylor Reynolds number of $\mathrm{Re}_\lambda = 22.4$. Instantaneous results are shown for spanwise mean of pressure values after $t = 4T$ and $t = 8T$, where T represents the time needed for flow-through of one length of periodic box. Pressure values are chosen for plotting as they are good indicators of the reflection in acoustic waves. As shown in Fig. 4 (a), after time $t = 4T$ the disturbance in the postshock flow pass through the exit boundary of the normal length of computational domain ($x_1 = 4\pi$) but do not reach the subsonic exit ($x_1 = 6\pi$) of the longer domain. It can be seen that the results obtained from normal length of computational domain with non-reflecting boundary conditions, match well to those obtained from a longer computational domain with no effect of exit boundary. As can be seen from Fig. 4(b), even for later times, there is no significant deviation between the results from a longer computational domain and normal computational domain.

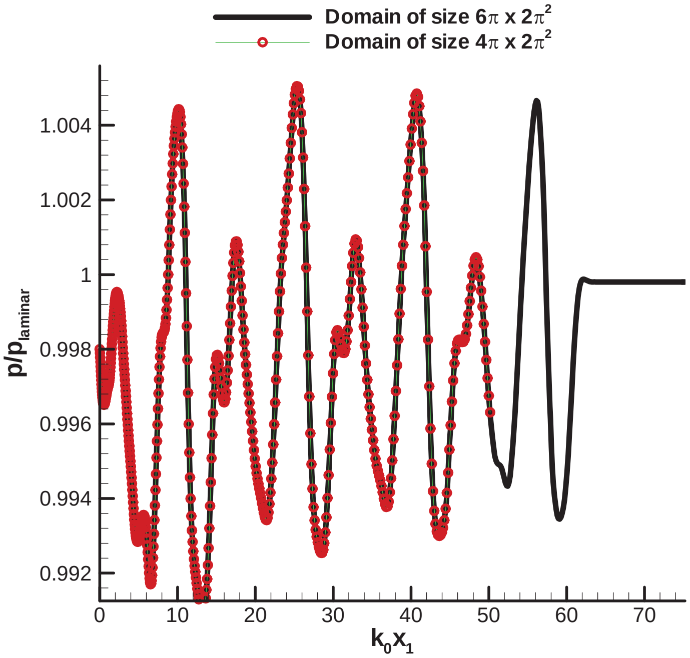

(a)

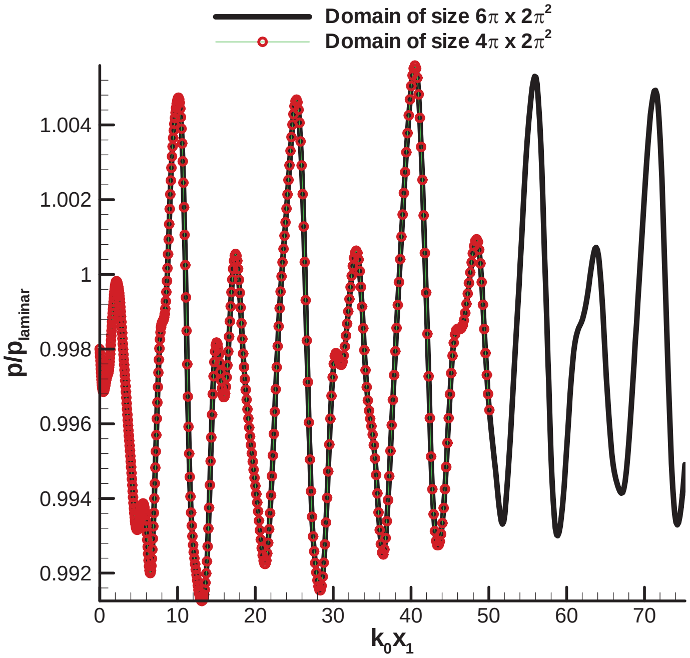

(b)

Fig. 4 Streamwise variation of instantaneous spanwise mean of pressure values obtained from two different sizes of computational domain using same inflow conditions after (a) 4 flow-through of inflow box and (b) 8 flow-through of inflow box.

It is also important to note that the region where significant statistical variations occur stays close to the shock-boundary. For computations of statistics, we need averaging over transverse directions as well as in time as the turbulence behind the shock is stationary and homogeneous in spanwise directions. We found that storing and computing averages from 60 instantaneous flow-fields during flow-through of one length of inflow box is necessary for statistical convergence.

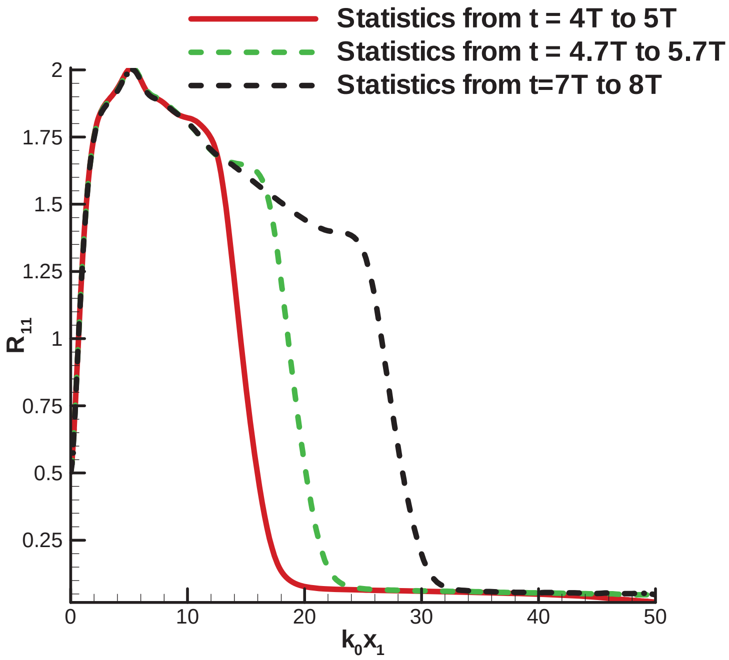

Fig. 5: Profile of streamwise-streamwise Reynolds stress computed using 60 snapshots of flow-fields at different points in time.

In Fig. 5, we show streamwise-streamwise Reynolds Stress, $R_{11} = \widetilde{u_1'' u_1''}$ (normalized by inflow Reynolds Stress), computed for one flow-through of inflow box at several different points in time. These calculations are for inflow conditions of $M_1 = 20$, $M_t = 0.126$ and $\mathrm{Re}_\lambda = 15.8$. All of these cases used 60 snapshots for averaging the statistics. It can be seen that statistics reach steady state in longer region behind the shock wave as time progresses. It was observed that for $M_1 = 20$, we obtain steady state in a region of length $25/k_0$ behind the shock after 8 flow-through lengths of the inflow. For lower Mach numbers, this region is larger. In our study, for most of the inflow cases, statistics are gathered for 8 flow-through lengths of the inflow and they were found to be converged for around half the computational domain behind the shock.

4.3 Computational Considerations: Grid Convergence

It is observed from shock-turbulence interaction simulations that turbulent fluctuations are generally much stronger just behind the shock. A typical distribution of density values in X-Y plane is shown in Fig. 6(a). Regions of highest gradients are observed just behind the shock while fluctuations attenuate moving towards the exit. Hence, to appropriately resolve the flow it is advisable to stretch the grid to cluster it near the shock wave. The grid-spacing in transverse direction is determined by the need to resolve all the lengthscales in DNS of turbulent flow.

DNS of the shock and turbulence interaction needs a large number of grids to fully resolve all the scales involved. For simulation of isotropic flows, it has been suggested [66] that one should resolve a wavelength of $4.5\eta_s$ where η_s is the Kolmogorov length scale for the flow in the computational domain. With our high order finite difference scheme such resolution will require a grid spacing of $2.0\eta_s$ in transverse direction. On the upstream side of the shock, the Kolmogorov length scale is defined as $\eta_0 \approx 0.51\lambda/\sqrt{\mathrm{Re}_\lambda}$. Larsson and Lele [36] have recently presented the relation for change in Kolmogorov length scale across the shock which leads to $\eta_s \approx \eta_0 (\rho_s/\rho_u)^{-11/8} (p_s/p_u)^{3/8}$ [74]. Assuming $\lambda \approx 2/k_0$, more than $6.1k_0\sqrt{\mathrm{Re}_\lambda}(\rho_s/\rho_u)^{11/8}(p_s/p_u)^{-3/8}$ grids are needed in transverse directions. Based on these requirements, we chose to use 128 grid points in transverse direction for the inflow Reynolds number of $\mathrm{Re}_\lambda = 6.2$ and Mach number $M_1 = 2-20$. While 256 grid points in transverse direction were found to be sufficient for $\mathrm{Re}_\lambda \leq 40.5$ and $M_1 = 2-20$.

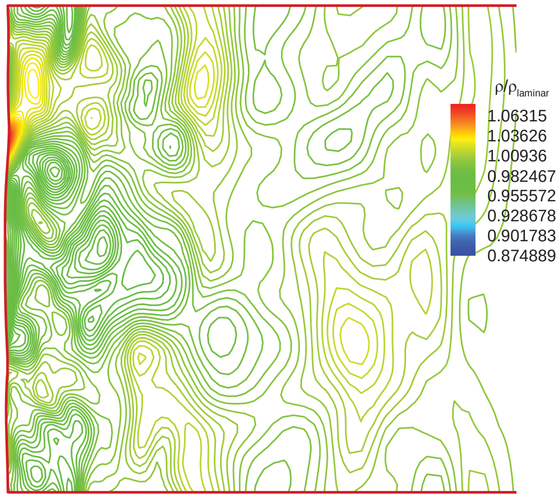

Fig. 6: Instantaneous iso-contours of density in X-Y plane at the top plane (Z=2π).

The grid convergence results for the highest Reynolds number case considered in this study are presented in Fig. 7 and Fig. 8. Convergence of inflow computation is presented in Fig. 7 presents result for the case $\mathrm{Re}_{\lambda 0} = 135$ and $M_{t0} = 0.175$ for three sets of grids: 128^3, 256^3 and 512^3. As an initial field for these computations, we first generate a randomized turbulence having desired spectra for the finest grids. The results are then spectrally filtered for coarse grid cases. This procedure is necessary to ensure spectrally same initial conditions for the decaying isotropic turbulence. It can be observed from Fig. 7 (a) that fairly converged values of turbulent Mach number are obtained for even the coarse grid for decaying isotropic turbulence. This was generally found to be true for the values of all the flow variables. However, the quantities involving the derivatives of the flow variables are seen to require more grid resolution. Skewness of streamwise velocity derivatives, S_1, is plotted in Fig. 7 (b) for the three sets of grids. The results from the coarsest grid 128^3 are within 5% of the finest grid results but converge to within 0.4% of the results from the finest grid as grids are doubled in each direction.

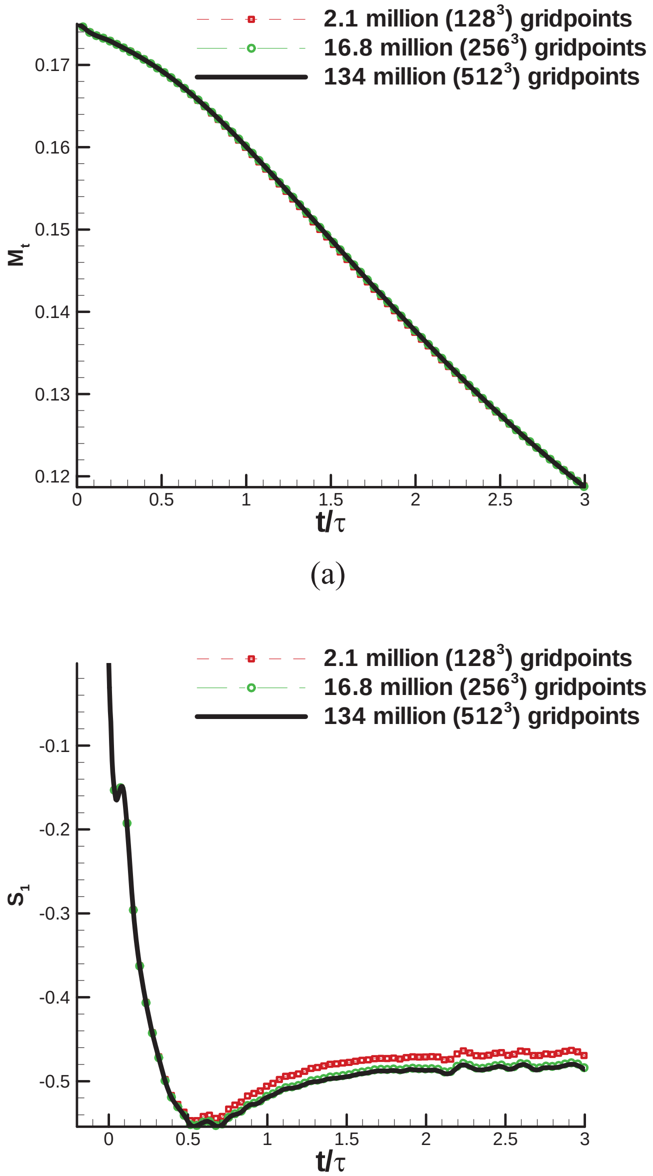

(a)

(b)

Fig. 7: Variation of (a) turbulent Mach number and (b) skewness of velocity derivatives with time in computation of isotropic decay of turbulence with three different sets of grids.

Similar to the inflow results, the main shock-fitting computations also show a better convergence for values of the variables as compared to the values of derivatives. These results are presented in Fig. 8 for various statistical quantities for three grids: 256×128^2, 512×256^2 and 1024×512^2. These grids use snapshots from decaying isotropic turbulence case of Fig. 7(a). The inflow conditions are: $M_1 = 4$, $M_t = 0.122$ and $\mathrm{Re}_\lambda = 40.5$. Results for variation of streamwise-streamwise Reynolds stress, $R_{11} = \widetilde{u_1'' u_1''}$ (normalized by inflow Reynolds Stress u_0^2) are shown in Fig. 8 (a). The results from all three grids are within 0.015% of each other.

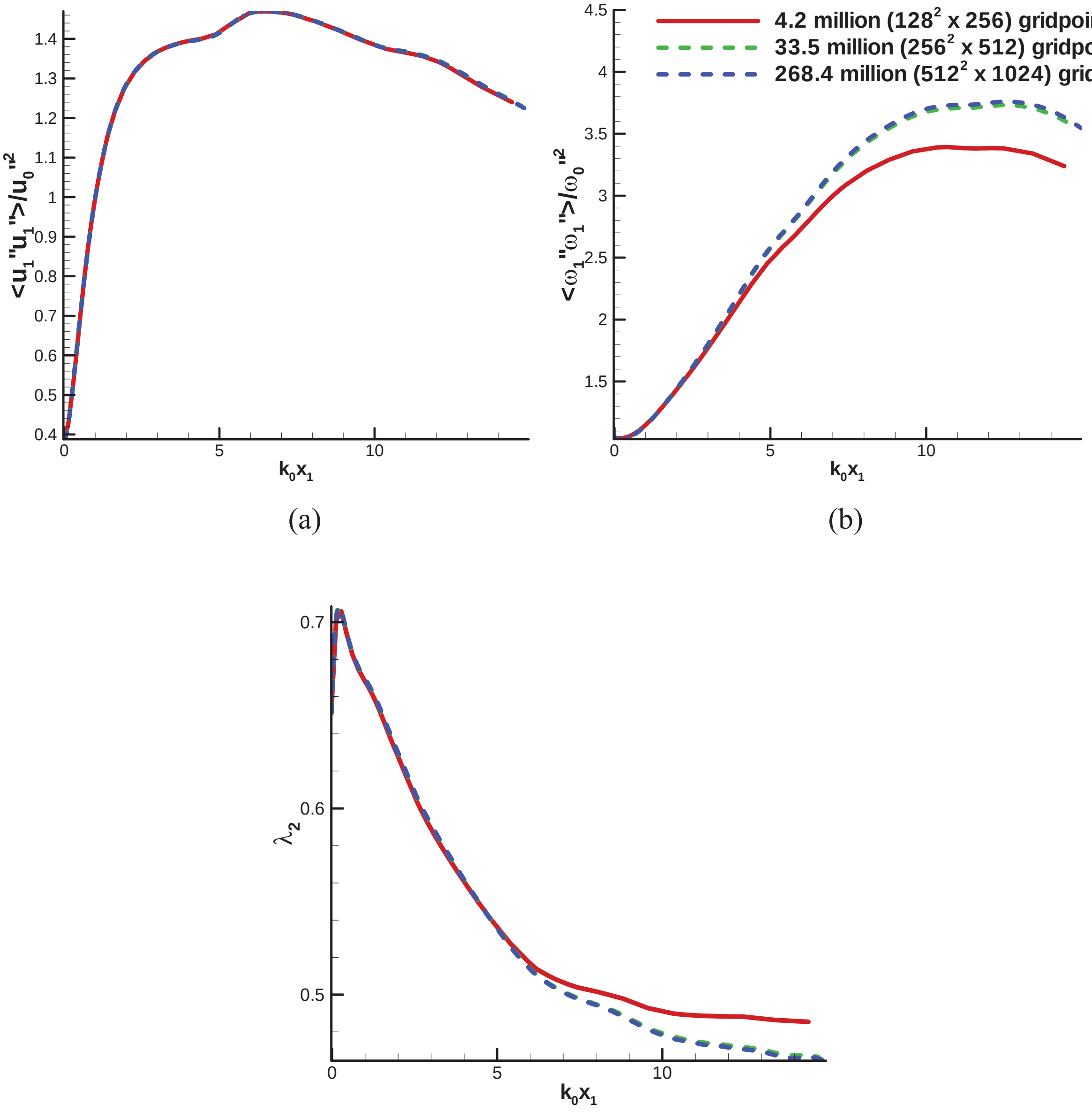

(a)

(b)

(c)

Fig. 8: Grid convergence of (a) variance of streamwise velocity, (b) variance of streamwise vorticity, and (c) transverse Taylor microscale in shock-fitting DNS of shock turbulence interactions.

Streamwise variation of of vorticity variance, $\widetilde{\omega_1''\omega_1''}$ is presented in Fig. 8(b). It is observed that there is significant difference between the results from the coarsest grid and the finest grid ($\sim 10\%$). The results obtained from 512×256^2 still stay within 1% of the finest grid. Similar results are obtained for transverse Taylor microscale as plotted in Fig. 8 (c). It should be noted that the value of mean inflow Mach number chosen puts most stringent requirement on the grid resolution. Increasing shock number beyond Mach 4 increases Kolmogorov scale in the post-shock flow and thus resolution requirements are relaxed. Based on these findings we use 512×256^2 grids for computing post-shock flow for all the cases having inflow Reynolds number in the range $10 \le \mathrm{Re}_\lambda \le 40.5$.

5 DNS RESULTS

As discussed in previous sections, the shock-fitting method is best utilized for incoming turbulence of low turbulence intensities interacting with very strong shocks. Reynolds number chosen for the incoming flow is constrained by the availability of computational resources. In this study, we present results from 7 different cases of inflow conditions which are listed in Table 1. We compute 4 cases of DNS computations with incoming flow of turbulence intensities $M_t \approx 0.12$ while varying mean Mach number from 2-20 and Reynolds number, Re_λ, from 6.2 to 40.5. These inflow conditions are listed as Cases I-IV. For $\mathrm{Re}_\lambda \approx 40$, we also compute 3 cases: Cases IV, V and VI, by varying the turbulent Mach number from 0.122 to 0.376 to observe the effects of increase in fluctuation amplitude. Case VII has turbulent Mach number and Reynolds number within the range of other cases.

Table 1: Cases of inflow conditions considered in this study.

	M_1	M_t	Re_λ	Grids
Case I	2 - 20	0.121	6.2	$128^2\times192$
Case II	2 - 20	0.126	15.8	$256^2\times512$
Case III	2 - 20	0.124	29.2	$256^2\times512$
Case IV	2 - 20	0.122	40.5	$256^2\times512$
Case V	2 - 20	0.185	38.4	$256^2\times512$
Case VI	3 - 20	0.376	39.7	$256^2\times512$
Case VII	2 - 20	0.275	22.4	$256^2\times512$

Results are presented here for the mean value of flow quantities along with some important statistics for post-shock flow. Following the literature, velocity and vorticity variances are considered along with Taylor miscroscales in the turbulent post-shock flow. Where possible, comparisons with previous numerical and theoretical studies have also been made. We have computed linear theory results based on analysis of Mahesh [20]. In this section, we use M_t and Re_λ to represent inflow values of turbulent Mach number and Reynolds number based on Taylor Microscale, respectively. Inflow values of variance of velocity fluctuations, $\widetilde{u_1^{"}u_1^{"}}$, is referred as u_0^2 in this section. Similarly, ω_0^2 has been used for denoting variance of vorticity fluctuations, $\widetilde{\omega_1^{"}\omega_1^{"}}$ in the incoming turbulence. Taylor microscale in the isotropic turbulence upstream of the shock is denoted as λ_{0u} in this section. Results are presented only for post-shock flows ($x_1 \ge 0$, assuming shock at $x_1 = 0$).

5.1 Mean Profiles

For the post-shock flows in shock turbulence interactions, the Linear theory results assume fluctuations around the mean values given by Rankine Hugoniot jump conditions. Lele [75] used results of rapid distortion theory (RDT) to find shock-jump relations in turbulent flows. A drift velocity in normal shock moving through a turbulent flow was found to be necessary to sustain the laminar density ratio corresponding to the stationary shock. This corresponds to a smaller jump in mean density and pressure of turbulence flow across the shock wave than that predicted by Rankine Hugoniot conditions. In the Fig. 9, we present the profiles of mean streamwise velocity, density and pressure behind the shock for inflow conditions of case IV. Mach number has been varied from 2 to 20. Just downstream of the shock wave mean values change rapidly. Mean velocity first decreases and then increases while mean values of density and pressure show a compression of the flow followed by expansion. As discussed earlier, sharp changes behind the shock waves are observed in instantaneous visualization of the flow as well and have lead us to use grid refinement near the shock. Similar profiles are observed in all the cases considered in this study. It is observed that, for all the cases, mean values of pressure and density behind the shock are lesser than those observed in corresponding laminar flow. These results are consistent with those reported in the literature [36]. We also observe from Fig. 9 that as mean Mach number value of incoming flow is increased at fixed value of turbulent Mach number and Reynolds number, the difference between laminar and turbulent post-shock mean values decreases. This observation was found to be true for all seven cases of inflow turbulence considered in this study.

To gauge effects of varying inflow turbulence parameters, mean values of density, streamwise velocity and pressure resulting from interaction of all seven inflow cases with a Mach 5 shock wave are presented in Fig. 10. Cases I, II, III and IV correspond to approximately same turbulent Mach number $M_t \approx 0.12$ but different Re_λ values ahead of the shock wave. Mean values of density and streamwise velocities for these cases are not much different from each other. On the other hand, changing M_t of the inflow has very pronounced effect on the deviation of turbulent mean values from corresponding laminar values. Higher turbulent Mach numbers at fixed value of mean Mach number lead to larger deviations from the laminar mean states. Effect of turbulent and mean Mach number values on mean profiles is consistent with RDT based prediction of Lele[75]. It should be noted that the results in this study are obtained by assigning laminar postshock pressure at the exit boundary since turbulent jump conditions are not known beforehand. This may be the reason the pressure values are observed to be increasing towards the laminar mean values downstream of the shock wave. However, the deviations from laminar values are very small (less than 1%) and specifying laminar value as exit pressure does not affect our solution, as discussed in previous section. From our results it seems that turbulence intensity or ratio M_t / M_1 is an important factor in determining the deviation from laminar values.

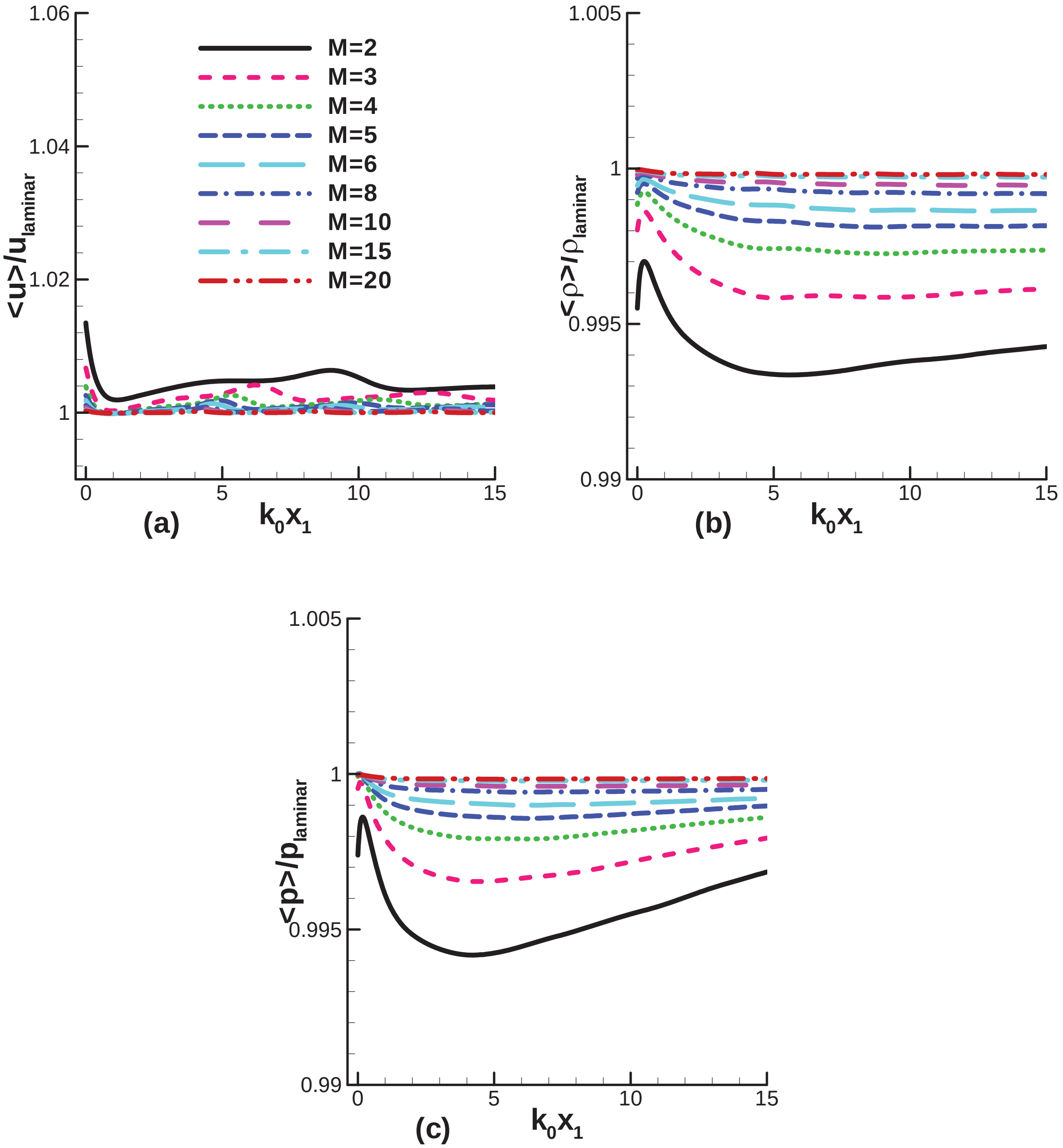

Fig. 9: Profile of mean values of (a) streamwise velocity, (b) density and (c) pressure for case IV ($\mathrm{Re}_\lambda = 40.5$, $M_t = 0.122$) behind the shock. All variables are normalized by respective laminar flow values.

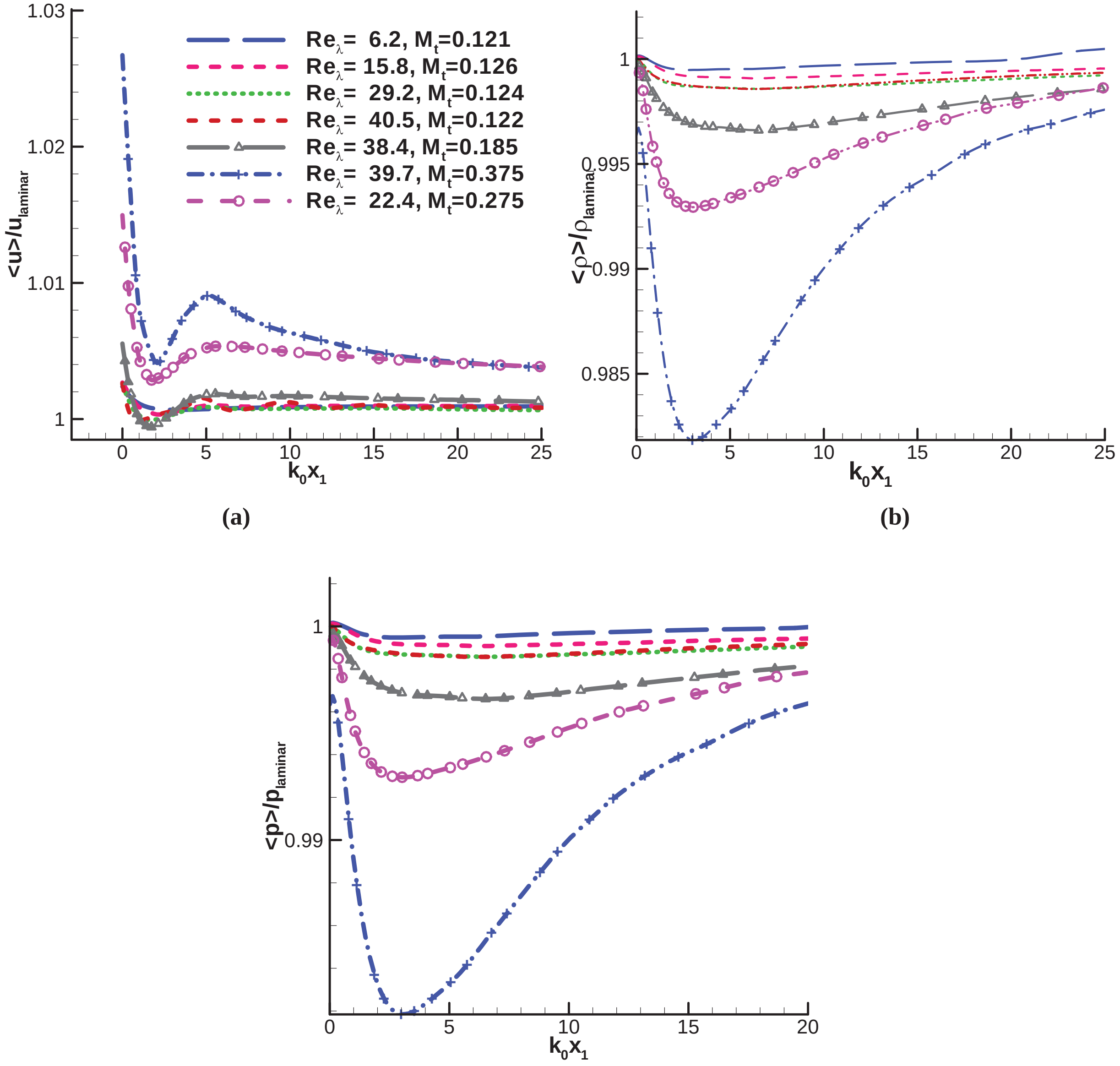

(a)

(b)

(c)

Fig. 10: Profile of mean values of (a) streamwise velocity, (b) density, and (c) pressure behind a Mach 5 shock wave for the seven cases of inflow turbulence listed in Table 1.

5.2 Fluctuations in shock-shape

The shock waves get distorted with the passage of turbulence. To estimate effects of variation in inflow turbulence on shock deformations, we plot root mean square values of the fluctuations in shock position, H_{rms}, in Fig. 11 for all seven sets of inflow parameters. The shock deformations for the Cases I, II, III and IV which have approximately same turbulent Mach number, $M_t \approx 0.12$, at inflow show little variation as Reynolds number Re_λ is changed. However, as we change turbulent Mach number of the incoming flow (Cases V, VI and VII), shock deformations increase appreciably. For all the cases, it is readily seen that increasing Shock-strength for a fixed turbulent Mach number, M_t, reduces the shock deformation.

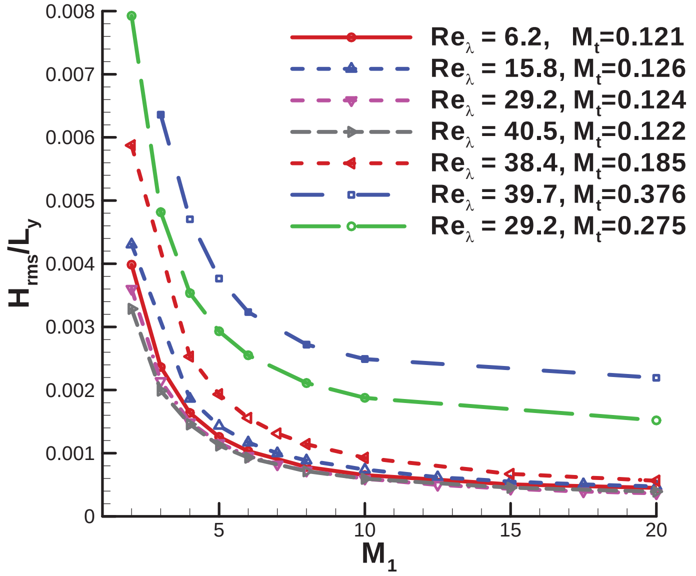

Fig. 11: Root mean square values of fluctuations in shock-shape.

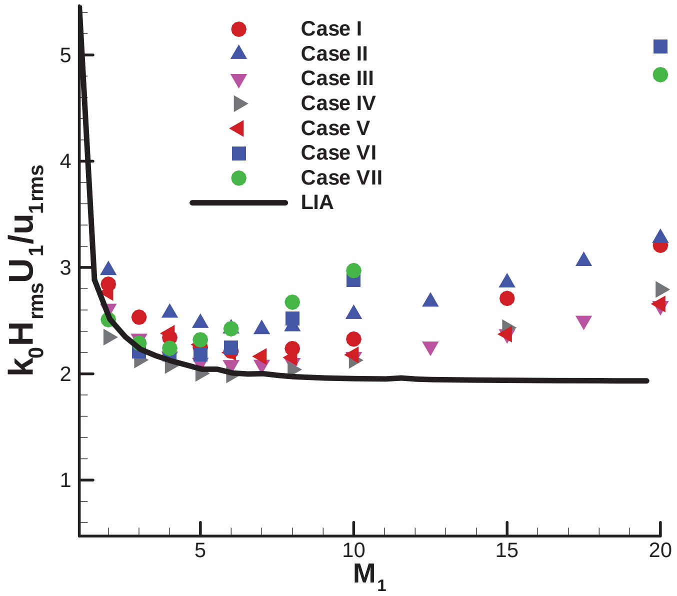

Fig. 12: Comparison with LIA for RMS values of fluctuations in shock-shape.

To further examine the dependence of shock deformation on inflow parameters, we also compute results using Linear Interaction Analysis (LIA) method of Mahesh [20]. The LIA results for RMS value of the shock fluctuations are compared with those obtained from this study in Fig. 12. The H_{rms} values has been scaled with $\overline{u_1'}/\left(k_0U_1\right)$, where U_1 is the mean streamwise velocity ahead of the shock. This scaling comes naturally from LIA. LIA predicts the parameter $H_{rms}k_0U_1/\overline{u_1'}$ to be approximately constant for stronger than Mach 2 shocks. This amounts to

H_{rms} being almost linearly proportional to the turbulence intensity $\overline{u_1'}/U_1$ (or M_t/M_1). The shock fluctuation predictions from LIA assume perfectly incompressible fluctuations in inviscid fluid. Our computations, on the other hand, solve relatively viscous flows using developed turbulence. Hence, small deviations from the LIA results are expected. However, as shown in Fig. 12, for small enough mean Mach number (less than Mach 6), the computational results follow the trend predicted by LIA and RMS value of shock deflections, H_{rms}, vary linearly with M_t/M_1. For stronger shocks, however, the difference between the linear theory and computations are seen to increase as mean Mach number of flow is increased. In general, for very strong shocks, it is seen that LIA underpredicts the shock displacement fluctuations.

5.3 Reynolds Stress

Linear interaction analysis (LIA) as well as DNS of shock turbulence interactions considered by various researchers [13, 76] show that turbulent velocity fluctuations are amplified across the shocks. Moreover, the amplification in turbulent kinetic energy is seen to saturate beyond Mach 3 shocks [1, 36]. In this study, we compare the shock-fitting results to those presented in the literature and extend the results to very strong shocks. For comparisons, we also present the results we computed using LIA theory of Mahesh et al. [20].

LIA results for evolution of the normal components of Favre's Reynolds stresses, $R_{ij} = \widetilde{u_i'' u_j''}$, behind the shock wave are plotted in Fig. 13 for $M_1 = 2.0$. The velocity fluctuations are observed to be axisymmetric behind the shock wave and non-diagonal components of Reynolds stress tensor, R_{ij}, were found to be close to zero. These values are also compared against those obtained from our shock fitting method for case I, i.e. inflow conditions corresponding to $M_1 = 2.0$, $\mathrm{Re}_\lambda = 6.18$ and $M_t = 0.121$. All the stresses are normalized by the upstream Reynolds stresses represented as u_0^2. Mean position of the shock wave is at $x_1 = 0$.

It is observed that the turbulent fluctuations in the streamwise directions are reduced immediately behind the shock wave while the fluctuations in the transverse velocity increase. Just behind the shock, the computed amplification of Reynolds stresses match well to those obtained from LIA. However, in the far field LIA results and computed results differ significantly as viscous decay of stresses was not taken into account in LIA. For both the LIA and computed results, the streamwise fluctuations rapidly evolve behind the shock until a length of $\sim 3/k_0$. This can be attributed mainly to the contribution of evanescent acoustic waves to the streamwise velocity just behind the shock. Maximum streamwise Reynolds stresses reached behind the shock in the computed flow are significantly smaller than those predicted by LIA. In the far field behind the shock fluctuations in all the velocities components decay because of viscous dissipation. Fluctuations in both the transverse velocity components, $\widetilde{u_2'' u_2''}/u_0^2$ and $\widetilde{u_3'' u_3''}/u_0^2$ almost coincide with each other pointing to the axisymmetry of turbulence behind the shock. As compared to the streamwise components, transverse components decay at a higher rate and the flow does not seem to return to isotropy in the far field. Similar observations have been reported in the previous studies [1, 4, 18, 36] in the literature. The results similar to those shown in Fig. 13 were obtained for low values of mean Mach number and turbulent Mach numbers. Effect of changing various inflow conditions is discussed in the ensuing text.

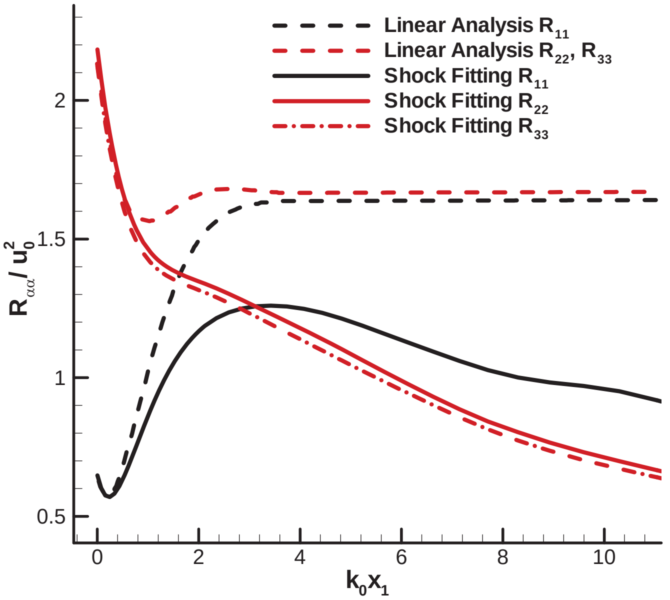

Fig. 13: Evolution of diagonal components of the Reynolds Stress tensor $R_{ij} = \widetilde{u_i'' u_j''} \big/ u_0^2$ behind the shock compared against those obtained from Linear Interaction analysis.

5.3.1 Effects of changing shock strength for fixed inflow turbulence.

LIA predicts that the amplification in turbulent kinetic energy saturates for stronger than Mach 3 shocks. Moreover, amplification of variance of streamwise velocity fluctuations (streamwise-streamwise Reynolds stresses, R_{11}) is expected to decrease beyond Mach 3 shocks. In past, simulations with very strong shocks have not been attempted to examine these theoretical results. We varied mean Mach number of the incoming flow from 2 to 20 for all cases of inflow conditions to see the effects of shock strengths on shock turbulence interactions. Streamwise variation of R_{11} for various shock strengths is presented in Fig. 14 for inflow conditions of case III ($\mathrm{Re}_\lambda = 29.2$, $M_t = 0.124$). Similar variations were observed in all the inflow cases considered in this study. For better representation of the trends we show effects of variation of shock strength on amplification of R_{11} in two parts. In Fig. 14(a), mean Mach number has been varied from 2 to 8. In general, the R_{11} values evolve rapidly behind the shock wave for all the shock strengths considered and reach maximum value before $x_0 = 10 / k_0$. It is observed that maximum value in amplification of streamwise velocity fluctuations decreases as the Mach number of the mean flow is increased till 8. The decrease in R_{11} is consistent with findings of LIA. This trend, however, reverses as shock strength is increased beyond Mach 8 as shown in Fig. 14(b). For stronger than Mach 8 shocks, the streamwise velocity fluctuations are amplified more as mean Mach number is increased. We also see that rate of decay of R_{11} / u_0^2 behind the maximum value decreases as the shock strength is increased till Mach 8 while it is almost constant for stronger than Mach 8 shocks. Similar effects of changing the mean Mach number were observed in all the inflow cases.

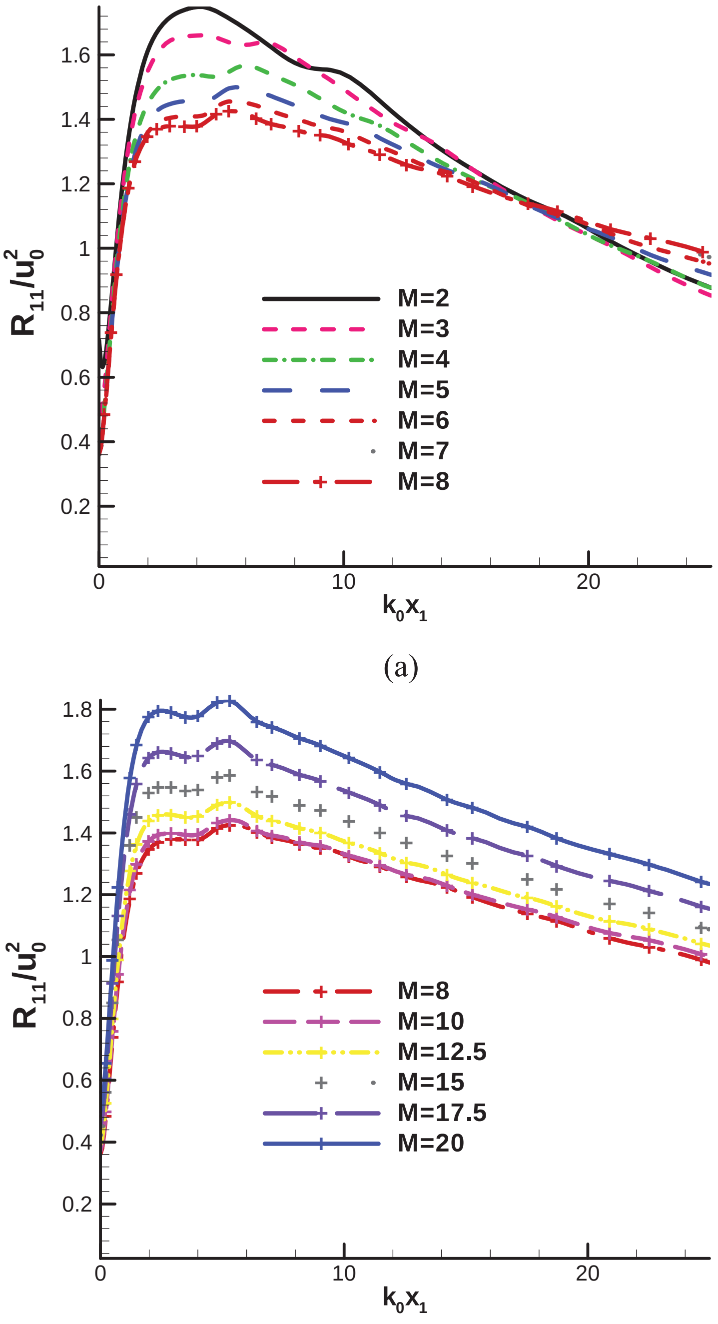

(a)

(b)

Fig. 14: Amplification in variance of streamwise velocity fluctuations for (a) $M_1 = 2-8$ and (b) $M_1 = 8-20$ for inflow conditions of case III ($\mathrm{Re}_\lambda = 29.2$, $M_t = 0.124$).

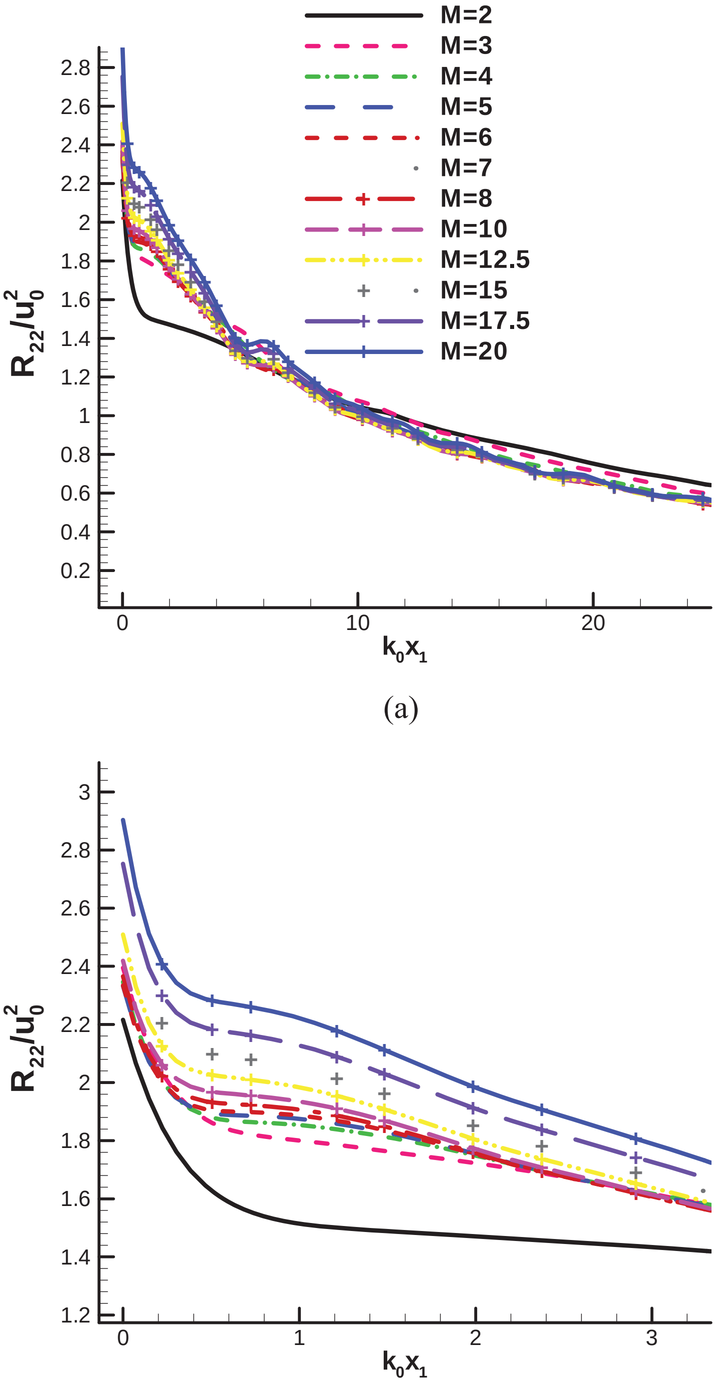

(a)

(b)

Fig. 15: (a)Amplification in variance of transverse velocity fluctuations for inflow conditions of case III case III ($\mathrm{Re}_\lambda = 29.2$ **,** $M_t = 0.124$ **) with varying Mach number. (b) shows a zoomed view just behind the shock.**

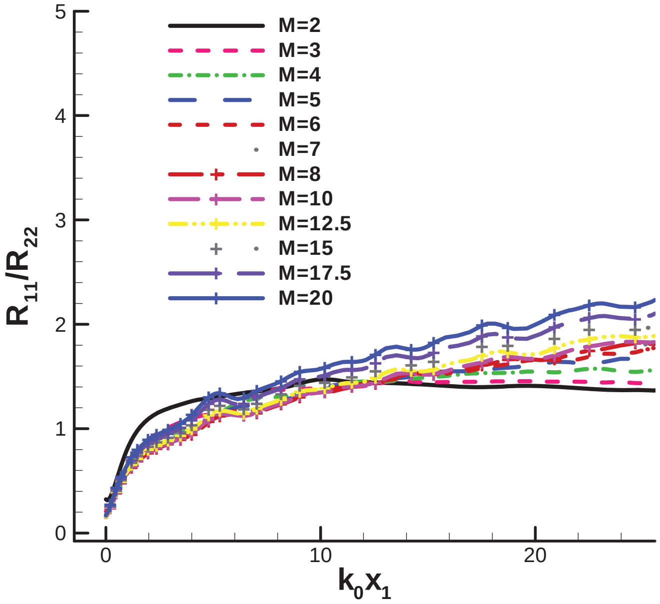

Fig. 16: Streamwise of variation of ratio R_{11}/R_{22} for case III ($\mathrm{Re}_\lambda = 29.2$, $M_t = 0.124$) for a number of varying mean Mach numbers.

Streamwise profile of variance of transverse velocity fluctuations for the same inflow conditions (case III) is shown in Fig. 15. Variance of transverse velocity fluctuations, R_{22}, is amplified by a factor of 2 to 3 across the shocks for $M_1 = 2-20$. As can be observed from Fig. 15, just across the shock, the amplification of transverse velocity fluctuations increases monotonically as mean Mach number of the incoming flow is increased. Downstream of the shock, R_{22} values decay continuously. The decay rate is higher for stronger shocks. As discussed for Fig. 13, interaction of isotropic turbulence creates anisotropy in the Reynolds stresses behind the shock leading to a higher value of R_{11} than R_{22} for all the cases computed. We quantify the anisotropy in the velocity fluctuations as ratio R_{11}/R_{22}. The anisotropy for the inflow conditions of case III are shown in Fig. 16. In the far-field, variance of streamwise velocity fluctuations is always greater than that observed for transverse fluctuations. Thus, velocity fluctuations remain anisotropic. When the mean Mach number is increased while keeping M_t and Re_λ fixed, the anisotropy in the far-field further increases.

5.3.2 *Effects of changing shock strength for fixed inflow turbulence.*

As discussed before, we compute shock turbulence interaction for seven different cases of inflow conditions. These inflow simulations are generated using separate simulations each starting with different random fluctuations. The only parameters we have controlled are Reynolds number and turbulent Mach number of the incoming flow. Effect of these different inflow conditions on the velocity fluctuations of turbulence past Mach 4 shock wave are shown in Fig. 17. Profiles of R_{11}/u_0^2 as shown in Fig. 17(a), show similar evolutions just behind the main shock for all the cases and are close to the values predicted by LIA. Further downstream, cases with low Re_λ values show sharp decay in amplitude of velocity fluctuations and maximum value of amplification reached is generally higher for less viscous post-shock flows. Effect of changing turbulent Mach number, M_t, on the fluctuations is not clear from the cases computed here. The peak value of amplification in R_{11} is not much different for cases having similar Reynolds numbers but different turbulent Mach numbers. Increase in M_t, however, forces a higher rate of spatial decay of streamwise velocity fluctuations. Fig. 17(b) presents effect of changing inflow turbulence on variance of transverse velocity fluctuations. Amplification and initial decay in the spanwise-spanwise Reynolds stress, R_{22}, is predicted well by the LIA computations. Unlike the inviscid results from LIA, the transverse velocity fluctuations keep decaying further downstream. Higher decay is again observed with the cases of higher viscosity. Effect of increasing turbulent Mach number of incoming isotropic fluctuations is to induce faster decay in R_{22}. These observations are representative of the results for smaller than Mach 8 flows.

In general, we observe that as the shock strength is increased, deviation from LIA results also increases. LIA predicts that amplification of turbulent kinetic energy should saturate for stronger than Mach 3 shocks. The results presented for R_{11} and R_{22}, however, show an increase in velocity fluctuations as mean Mach number is increased. A direct comparison of computed streamwise Reynolds stresses with those obtained from LIA is not straightforward. It should be noted that, unlike LIA results, the streamwise-streamwise Reynolds stress R_{11} decays downstream of the shock. Hence, it is not clear which far-field value from the computations should be chosen for comparison with the LIA results. Researchers in past have made comparisons with LIA by extrapolating the R_{11} values to the shock location [36]. The LIA results, however, spatially evolve behind the shock as well and are not same at shock location and far-field. Therefore, we do not extrapolate our results to the shock location for comparison. Since the values in the far-field are expected to be affected by viscosity, it is best to compare the values of velocity fluctuations just behind the shock, i.e. at $x_1 = 0$. This comparison is presented in Fig. 18. Here, we also plot values from earlier studies of Lee et al. [1] and Jamme et al. [4]. For low values of turbulent Mach numbers, our results match well to those obtained from LIA. Cases Ĉ□□□□□□□□□□□□□□□□Ĉ□□□□□□Ĉ□□□□□J□Ĉ□□□□й□Љ□Љ□□□□□□□□r, are close to the LIA results only for weaker than Mach 6 shocks. With the stronger shocks, there are strong non-linear effects leading to large deviation from LIA in results for these two cases. These results are consistent with the observations for shock fluctuations.

We also find the maximum postshock values of R_{11}, R_{22} and turbulent kinetic energy, $\widetilde{u_i''u_i''}$ for all the cases computed and compare them against the LIA results. The maximum R_{11}/u_0^2 values for different cases are plotted against far-field values in LIA results in Fig. 19. We also plot results from Larsson et al. [36], Lee et al. [1] and Jamme et al. [4] for comparisons. It should be noted that results by Larsson et al. [36] were obtained by extrapolating the velocity variances to the shock position. Their results are presented here as guideline only. Extrapolated values are expected to be higher than the maximum value in the far-field. We do not plot the Cases VI and VII from our computations for the sake of better presentation. As discussed previously, strong non-linear effects are noted for those two cases leading to high values of amplification in streamwise velocity fluctuations for very strong shocks. We observe from Fig. 19 that LIA results predict that amplification in streamwise vorticity should slowly decrease as mean Mach number is increased beyond 2. Previous studies [1, 4, 36], carried out for weaker than Mach 6 shocks, support this argument. Our results in the same Mach number range also show a decrease in maximum amplification of streamwise velocity fluctuations. However, for stronger than Mach 8 shocks this trend reverses and we observe increased amplification of streamwise velocity fluctuations for stronger shocks.

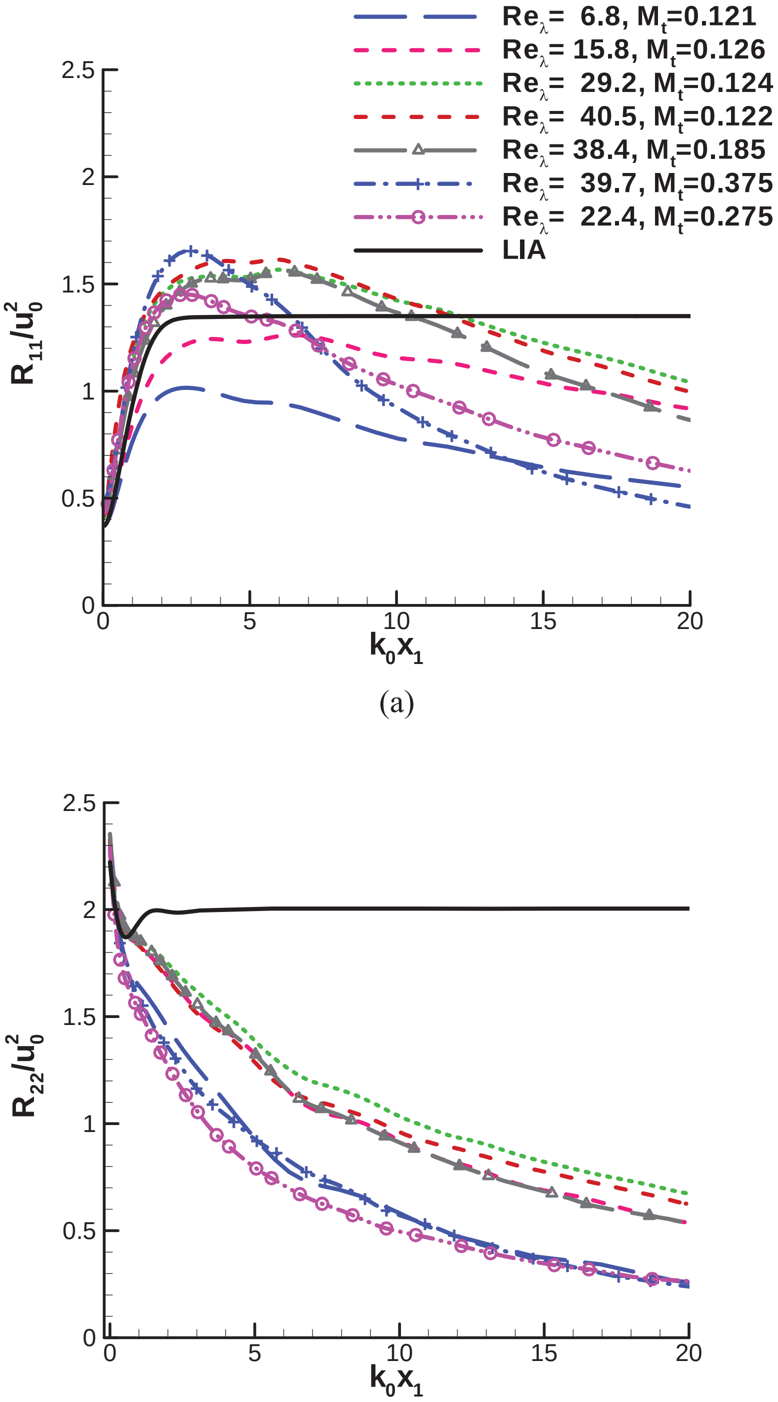

(a)

(b)

Fig. 17: Amplification of variances of (a) streamwise velocity and (b) spanwise velocity for seven different cases of inflow turbulence on interaction with a Mach 4 shock.

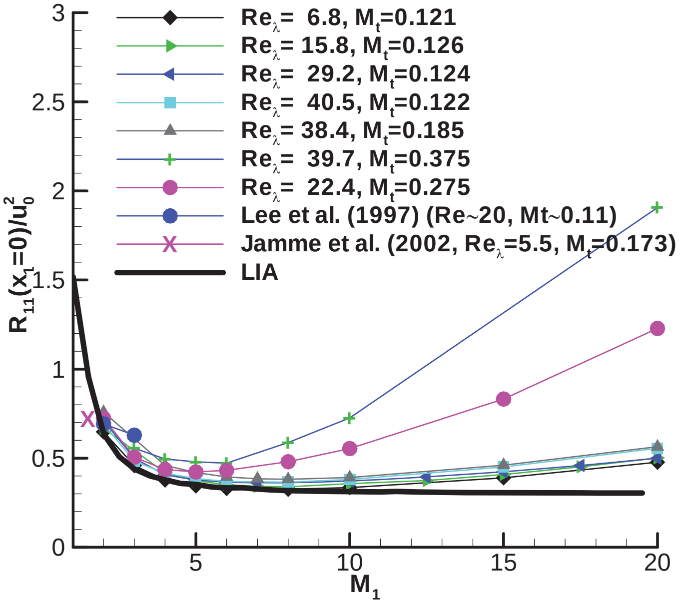

Fig. 18: Comparison of results from present work, LIA and those available in literature for amplification of variance of streamwise velocity fluctuations just across the shocks of different shock-strengths.

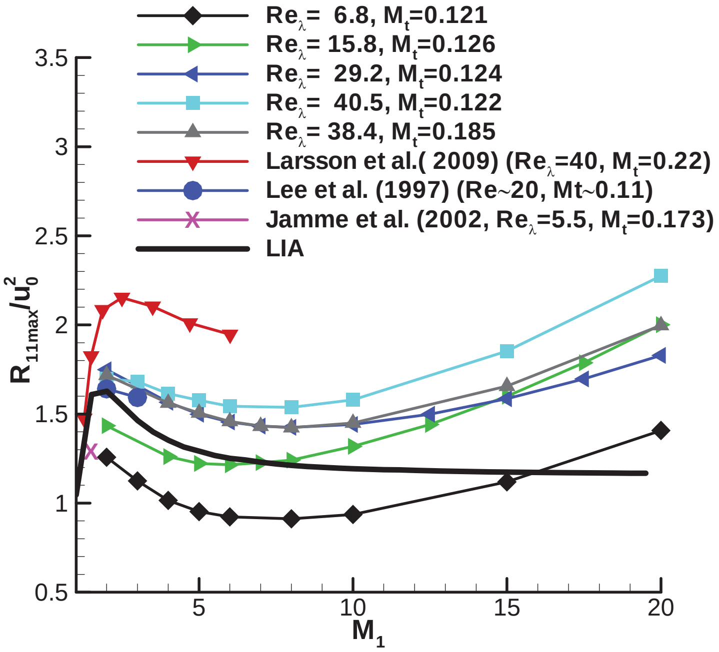

Fig. 19: Comparison of maximum value of R_{11}/u_0^2 downstream of the shock wave as obtained from present work, LIA and those reported in literature.

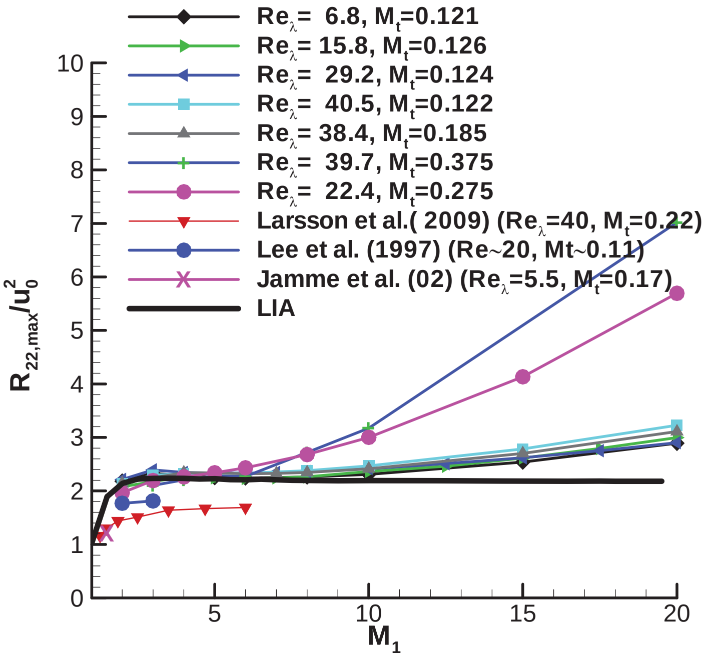

Fig. 20: Comparison of amplification in variance of transverse velocity fluctuations across the shocks of different strengths as obtained from present work, LIA and those available in literature.

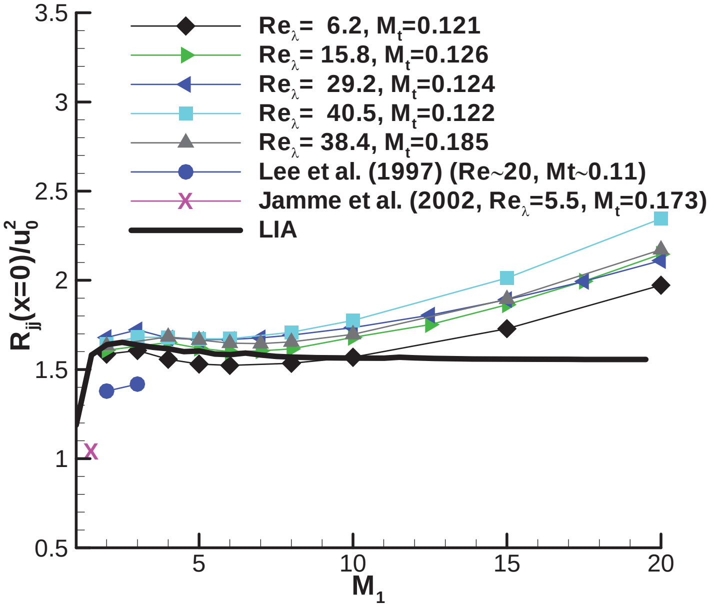

Fig. 21: Comparison of amplification in turbulent kinetic energy across the shocks of different strengths as obtained from present work, LIA and those available in literature.

Maximum variance of transverse velocity fluctuations and turbulent kinetic energy is achieved just behind the shock. Result for transverse velocity fluctuations are shown in Fig. 20. It is again evident that the shock-fitting results follow LIA results for weak shock waves but consistently show higher values than that predicted by LIA for stronger than Mach 7 shocks.

Consistent with results of the velocity fluctuations, turbulent kinetic energy amplification is predicted well by LIA for weaker than Mach 8 shocks, as shown in Fig. 21. We observe an increase in turbulent kinetic energy for stronger shocks while LIA predicts a constant value. Computations of shock-turbulence interaction problems for such Mach numbers have not been undertaken in past and hence such trends have never been observed. Current study supports the findings by previous researchers for lower Mach number flows but also finds new trends for the flow regimes that were never considered before.

5.4 Vorticity variance

For the quasi-incompressible inflow turbulence considered in this study, one of the most important contributions to the dissipation of turbulent kinetic energy is expected from the vorticity fluctuations. A typical postshock evolution of the variance of the different components of vorticity fluctuations, $\widetilde{\omega''_\alpha \omega''_\alpha}$, behind the shock is presented in the in Fig. 22 for the inflow conditions: $M_1 = 3.0$, $Re_\lambda = 40.5$ and $M_t = 0.122$. It can be seen that, as expected, interaction of isotropic turbulence creates axisymmetric field in vorticity downstream of the shock. We observe that the streamwise vorticity fluctuations do not change significantly as the flow passes through the shock. This is in accordance with the linear theory and results obtained in previous studies [1, 18, 36]. On the other hand, transverse vorticity fluctuations are significantly amplified just behind the shock. For the case shown in Fig. 22, we observe that fluctuations in streamwise vorticity increase further downstream of the shock while variance of transverse vorticity monotonically decays behind the shock. Eventually, vorticity fluctuations become isotropic behind the shock. This confirms the recent DNS results [36, 37] and supports the argument that the smallest scales in flow behind the shock return to isotropy.

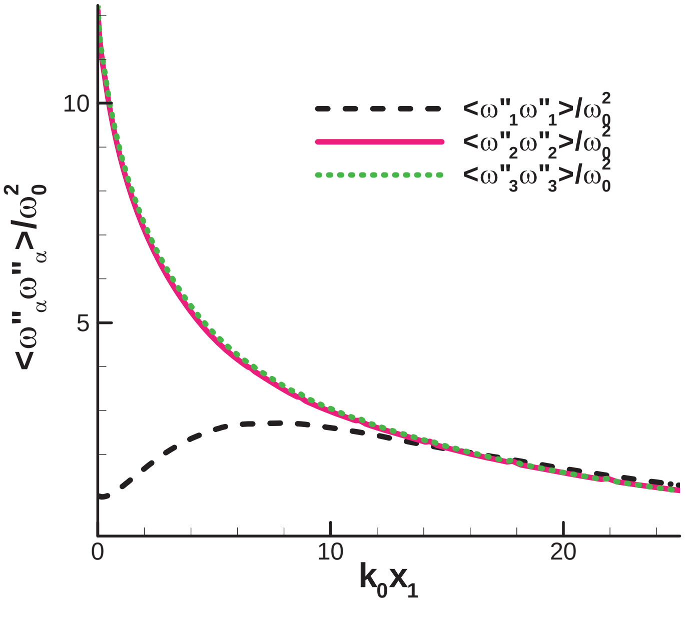

Fig. 22: Streamwise variation of variances of vorticity components for inflow parameters: $M_1 = 3.0$**,** $Re_\lambda = 40.5$ **and** $M_t = 0.122$**.**

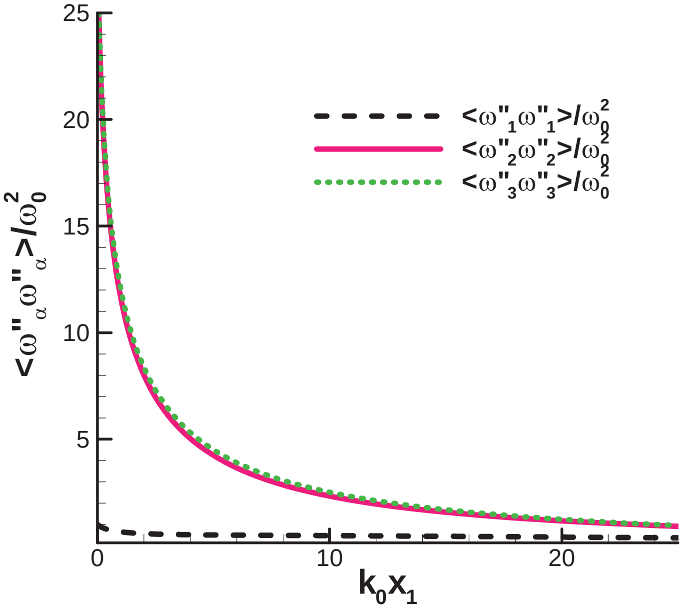

Fig. 23: Streamwise variation of variances of vorticity components for inflow parameters: $M_1 = 20.0$, $Re_\lambda = 40.5$ and $M_t = 0.122$.

Nature of vorticity fluctuations in the post-shock flow vary greatly depending on the characteristics of the incoming flow. For example, in the cases of low Reynolds number and high mean Mach numbers, return of vorticity values to isotropy is not clearly evident. Variances of streamwise and transverse vorticity components for incoming flow of mean Mach number 20 for same inflow turbulence as Fig. 22 are plotted in Fig. 23. Streamwise vorticity is unchanged across the shock wave but decreases further downstream and remains smaller than transverse vorticity over the computed domain. A discussion on effect of various inflow parameters on the variance of vorticity fluctuations is given in the following paragraphs.

5.4.1 Effects of changing shock strength for fixed inflow turbulence.

LIA predicts an increase in the transverse vorticity values which are expected to remain constant downstream of the shock. Amplitude of streamwise vorticity fluctuations is expected to remain unchanged throughout the computational domain. We observe these trends at the shock. However, downstream of the shock considerable non-linear effects are observed since both streamwise and transverse vorticity values change significantly moving away from the shock wave. Evolution of variance in streamwise vorticity fluctuations, $\widetilde{\omega_1''\omega_1''}$, is presented in Fig. 24 with the varying shock strengths but using same inflow turbulence of case III ($\mathrm{Re}_\lambda = 29.2$, $M_t = 0.124$). We see that, for weaker than Mach 8 shocks, streamwise vorticity increases behind the shock. Such increase is attributed to the non-linear tilting and stretching of vorticity and has also been reported in the past studies [18, 36]. We see that maximum values achieved by variance of streamwise vorticity fluctuations first increase and then decrease as the shock strength is increased. For the inflow of case III, as presented in Fig. 24, maximum peak streamwise vorticity fluctuations are observed for turbulence interactions with Mach 3 shocks. In past, researchers [18, 36] considered weaker than Mach 3 shocks for such comparisons and concluded that effect of increasing shock strength is to simply increase the amplification of streamwise vorticity fluctuations. While our results agree to these trend for lower Mach numbers, we see that for stronger than Mach 3 flows there is a decrease in streamwise vorticity. It is observed that beyond Mach 10 shocks non-linear tilting and stretching is suppressed by the viscous dissipation and streamwise vorticity continuously decreases downstream of the main shock.

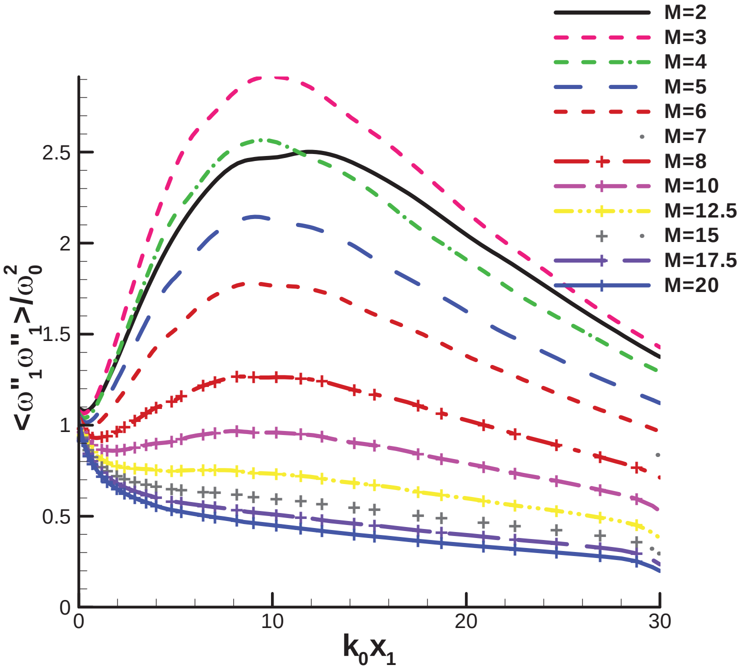

Fig. 24: Effect of increasing mean Mach number on variance of streamwise vorticity for inflow of Case III ($\mathrm{Re}_\lambda = 29.2$ **and** $M_t = 0.124$ **).**

We observe that effect of increasing shock strength on the streamwise vorticity values is also dependent on the inflow conditions being used. Effect of viscosity, in particular were seen to be very prominent in determining the variation of streamwise vorticity behind the shocks. As compared to Case III, inflow from Case I has lower Reynolds number while that from Case IV has a higher Reynolds number. Both of these cases have similar turbulent Mach number of incoming fluctuations. Effect of shock strength on the post-shock streamwise vorticity for these two cases are presented in Fig. 25 and Fig. 26, respectively. As shown in Fig. 25, for a lower Reynolds number case (Case I: $\mathrm{Re}_\lambda = 6.2$), it is clearly seen that the streamwise vorticity fluctuations are never amplified. This is because of very strong viscous effects. Jamme et al. [4] also observe a constant decay in the streamwise vorticity for cases having similar Reynolds number. We observe that increasing Mach number increases decay in the streamwise vorticity fluctuations for strongly viscous case. As Reynolds number of the inflow is increased, viscous dissipation becomes less dominant. Variation of streamwise vorticity fluctuations with changing mean Mach number is presented for higher Reynolds number case (Case IV: $\mathrm{Re}_\lambda = 40.5$) in Fig. 26. Similar to the results of Case III, streamwise vorticity values are amplified downstream of the shock wave of mean Mach number less than 10. As mean Mach number of the incoming flow is increased, the maximum value of variance of streamwise vorticity fluctuations in post-shock flow first increases and then decreases. For the inflow conditions of Case IV, the maximum amplification in streamwise vorticity fluctuations decreases for stronger than Mach 4 shocks.

This reversal in trend was noted beyond Mach 3 shocks (Fig. 24) for the inflow of case III. Thus, lower viscosity seems to enable amplification in streamwise vorticity for stronger shocks.

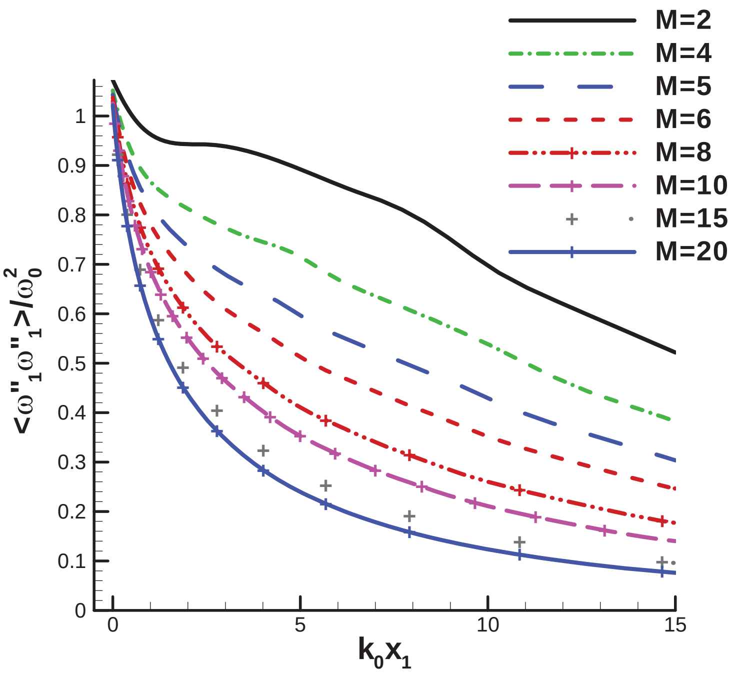

Fig. 25: Effect of increasing mean Mach number on variance of streamwise vorticity for inflow of Case I ($\mathrm{Re}_\lambda = 6.2$ and $M_t = 0.121$).

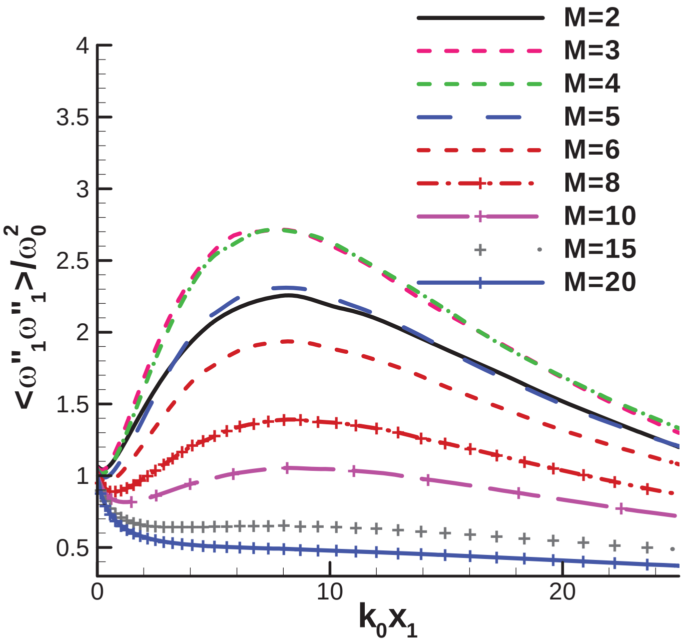

Fig. 26: Effect of increasing mean Mach number on variance of streamwise vorticity for inflow of Case IV ($\mathrm{Re}_\lambda = 40.5$ and $M_t = 0.122$).

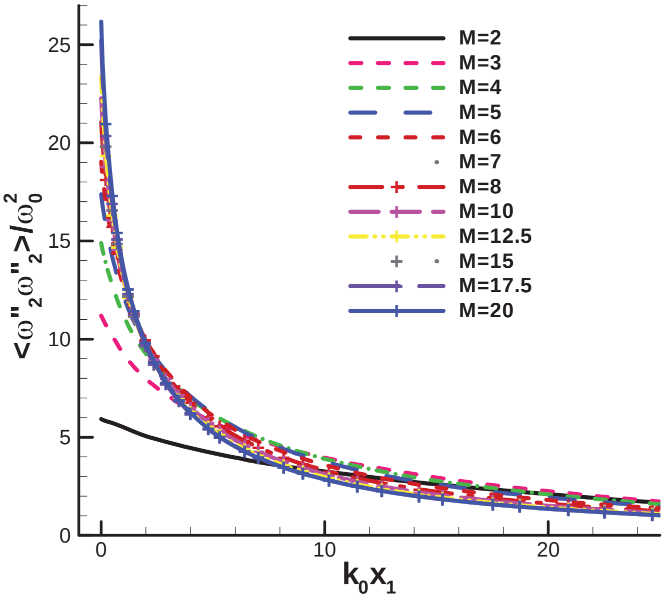

Fig. 27: Effect of increasing mean Mach number on variance of transverse vorticity for inflow of Case III ($\mathrm{Re}_{\lambda} = 29.2$ and $M_t = 0.124$).

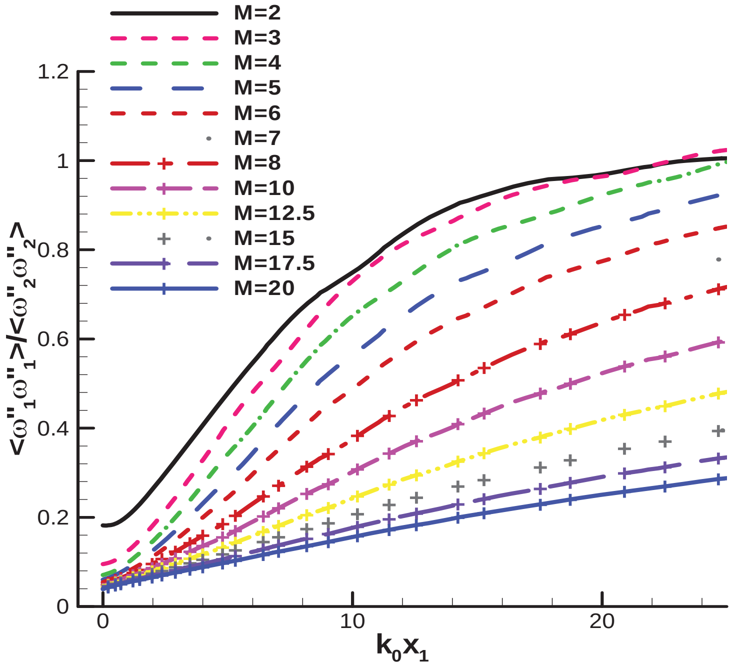

Fig. 28: Effect of increasing mean Mach number on anisotropy in vorticity fluctuations values for inflow of Case III ($\mathrm{Re}_{\lambda} = 29.2$ and $M_t = 0.124$).

Transverse vorticity fluctuations are considerably amplified after interaction with the shock as predicted by LIA and noted by several researchers [1, 18, 36, 37]. The transverse vorticity values are seen to decay monotonically behind the shock wave. Effect of changing mean Mach number on variation of transverse vorticity is shown in Fig. 27. Increasing the mean Mach number leads to higher amplification in the transverse vorticity fluctuations as predicted by LIA. The spatial rate of decay in variance of transverse vorticity is seen to increase as the mean Mach number is increased. Consequently, far-field amplification of transverse vorticity is smaller for stronger shock waves. Such observations were made for all the inflow cases considered in this study. As noted before, the vorticity values return to isotropy behind the shock for some cases. The ratio of variances in streamwise fluctuations to the transverse fluctuations, $\widetilde{\omega_1''\omega_1''} \big/ \widetilde{\omega_2''\omega_2''}$, can be used as a measure of anisotropy. Streamwise variation of this ratio is presented in Fig. 28 for the inflow of Case III. For stronger than Mach 3 shocks, we see that the return to isotropy behind the shock is delayed as the strength of the shock is increased.

5.4.2 *Effects of changing inflow conditions at fixed shock strength*

To examine the effect of varying turbulent Mach number and Reynolds number of the flow, we computed seven different inflow cases listed in Table 1 with shock waves of varying strengths. Results are presented here for interaction with a Mach 5 shock wave. Variance of streamwise vorticity fluctuations for these cases with incoming flow with mean Mach number of 5 is presented in Fig. 29(a). As stated before, effect of changing Reynolds number while keeping the turbulent and mean Mach number at a constant value is to increase the streamwise vorticity fluctuations downstream of the shock. There is actually no amplification observed for very low Reynolds number flows. As turbulent Mach number is increased, peak value of variance of streamwise vorticity fluctuations increases. Moreover, evolution of vorticity fluctuations is much faster behind the shock for the higher values of turbulent Mach numbers. Effect of changing inflow turbulence on anisotropy in vorticity fluctuations is presented in Fig. 29(b). It is again confirmed that effect of increasing Re_λ values in the flow is to delay the return to isotropy. An increase in turbulent Mach number of the incoming flow seems to hasten the return to isotropy behind the shock wave.

We have also implemented LIA of Mahesh et al.[20] to compute the vorticity fluctuations in the flow. We compare amplifications in transverse vorticity fluctuations from all of the computed cases to those from LIA study in Fig. 30. Results from Lee et al.[1] and Jamme et al.[4] are also plotted for comparisons. We observe that, similar to the previous studies, shock-fitting results are within 5% of the LIA results for weaker than Mach 8 shocks when turbulent Mach number is low. The cases with higher turbulent Mach number in inflow, diverge from the LIA results beyond Mach 5 shocks. It again seems that LIA is not sufficient for prediction of shock turbulence interactions for very strong shocks.

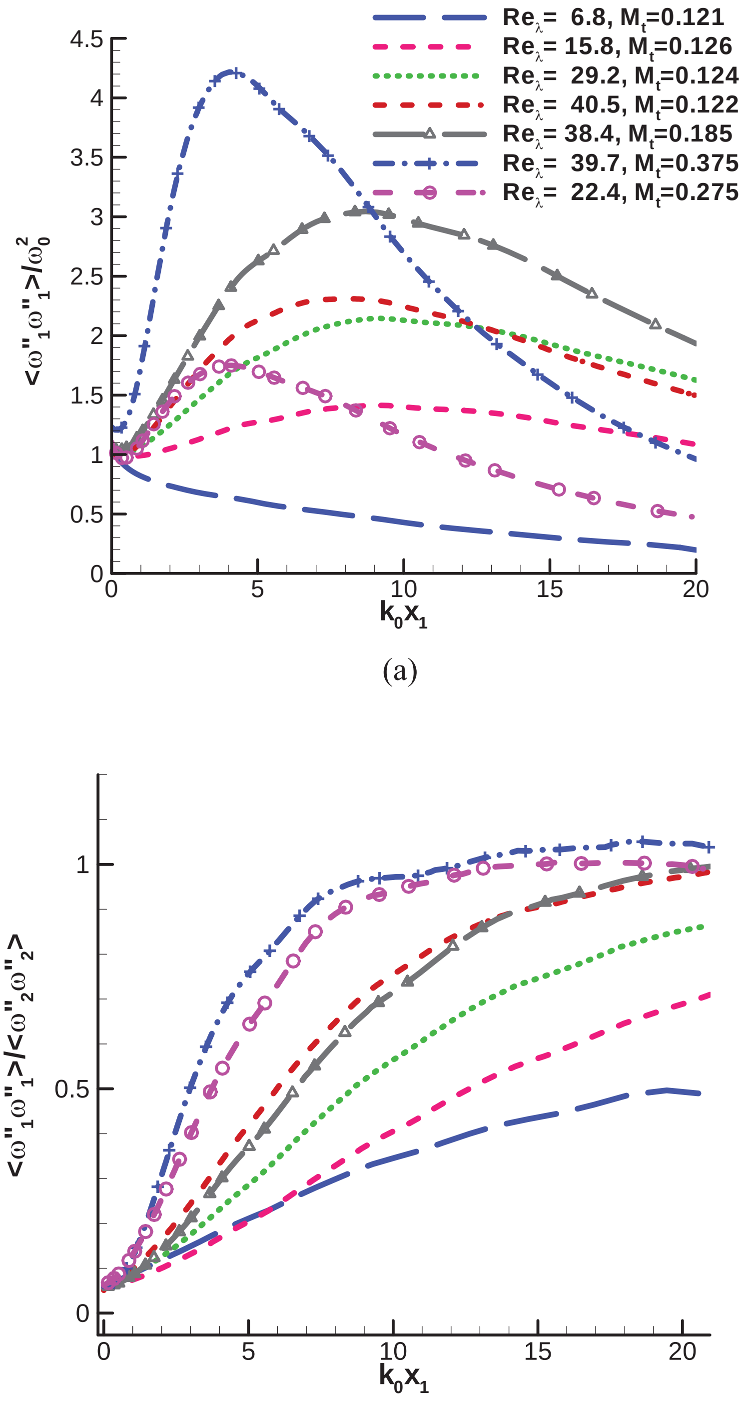

(a)

(b)

Fig. 29: Amplification of variances of (a) streamwise vorticity and (b) spanwise vorticity for seven different cases of inflow turbulence on interaction with a Mach 5 shock.

To sum, observations in this section point to the fact that viscous dissipation of streamwise vorticity is the main cause of anisotropy of the vorticity fluctuations. When incoming fluctuations with high enough turbulent intensities, $M/(\sqrt{3}M_t)$, can overcome the viscous dissipation we see an increase in streamwise vorticity values and return to isotropy. This result can be very important for turbulence modeling of such flows. In real life and lab experiments the Reynolds number observed are much higher than those considered in this study and for purpose of developing models one can assume the vorticity fluctuations to be isotropic downstream of the shock.

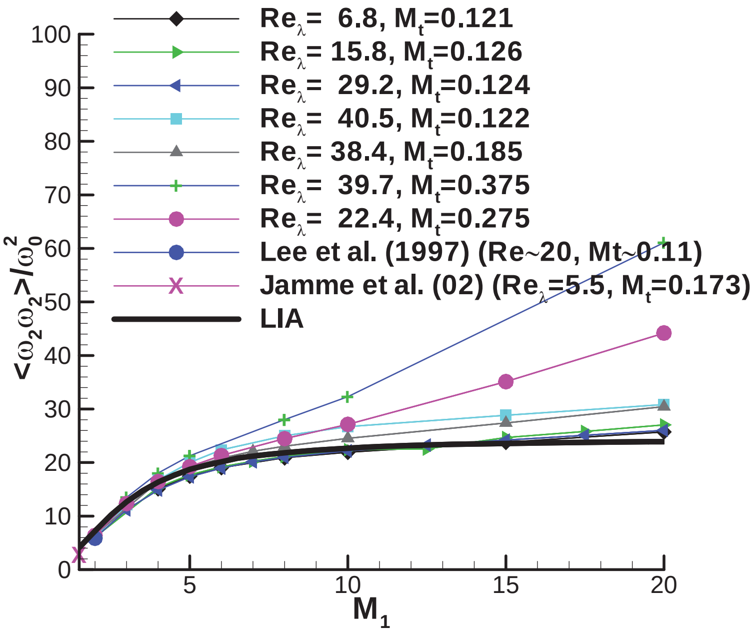

Fig. 30: Comparison of amplification in transverse vorticity fluctuations across the shocks of different strengths as obtained from present work, LIA and those available in literature.

5.5 Taylor Microscales

In almost all of experimental studies, turbulent microscales show an overall increase of the microscales during the interaction with normal shock [77]}. This is in contradiction with LIA and previous numerical studies [1, 4] which report decrease in Taylor microscales across the shock waves. In this study, we also found similar results. Typical profiles for evolution of Taylor microscales, λ_1, λ_2 and λ_3, across the shock wave is presented in Fig. 31 for inflow conditions: $M_1 = 2.0$, $\mathrm{Re}_\lambda = 40.5$ and $M_t = 0.122$. All the microscales are normalized by the value of Taylor microscale, $\lambda_{0,u}$, immediately upstream of the shock in the isotropic turbulent flow. It can be observed in Fig. 31 that all the microscales decrease significantly as the flow passes through the shock. The streamwise microscale, λ_1, is much smaller than the transverse microscale, λ_2, immediately downstream of the shock. However, λ_1 rapidly evolves further downstream while increase in λ_2 is not as pronounced. Transverse microscale, λ_2, remains less than the upstream value, $\lambda_{0,u}$, in all the cases computed in this study. These results correspond well with the recent results of Larsson et al.[36].

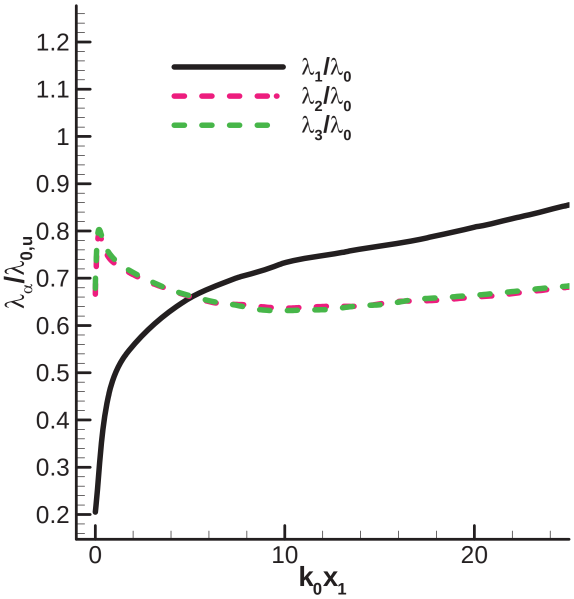

Fig. 31: Taylor microscales for inflow of $M_1 = 2.0$**,** $\mathrm{Re}_\lambda = 40.5$ **and** $M_t = 0.122$**.**

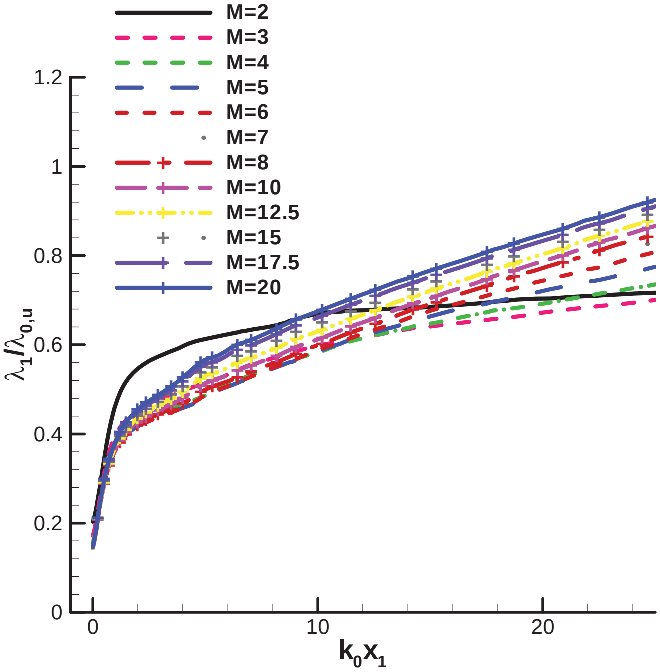

Fig. 32: Effect of increasing mean Mach number on streamwise Taylor microscale for inflow of Case III ($\mathrm{Re}_\lambda = 29.2$ **and** $M_t = 0.124$**).**

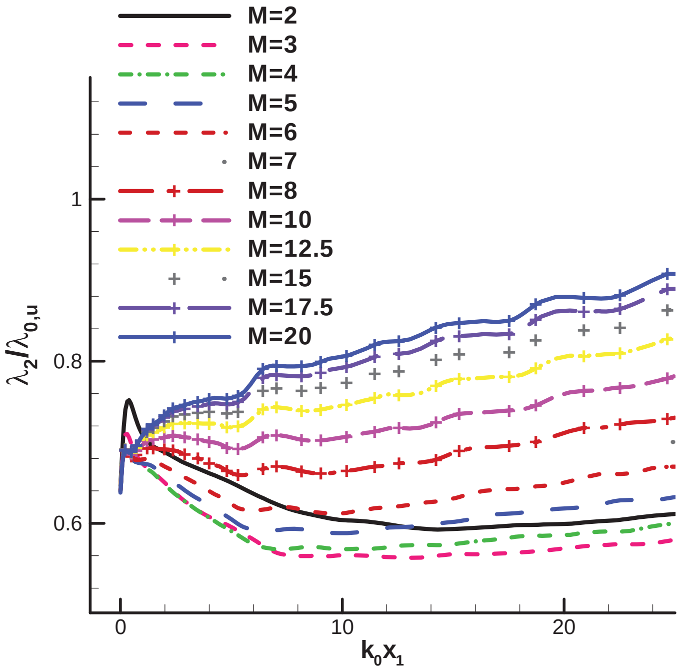

Fig. 33: Effect of increasing mean Mach number on transverseTaylor microscales for inflow of Case III ($\mathrm{Re}_\lambda = 29.2$ and $M_t = 0.124$).

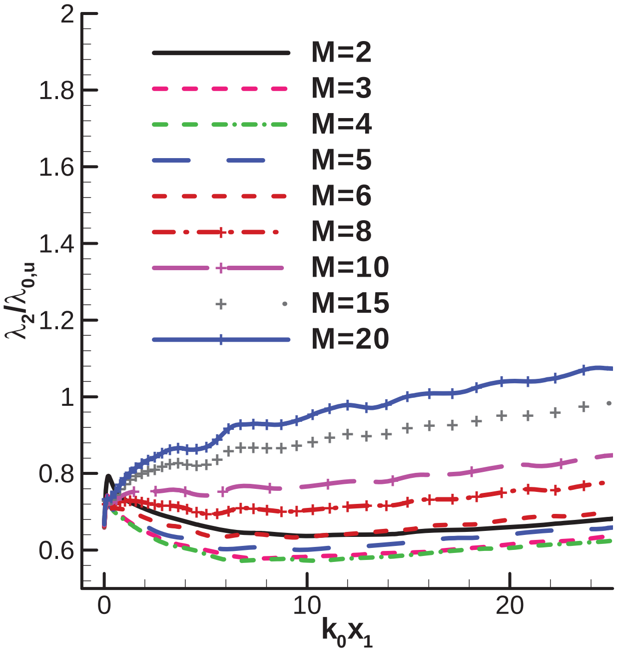

Fig. 34: Effects of increasing mean Mach number on transverse Taylor microscale for inflow of Case IV ($\mathrm{Re}_\lambda = 40.5$ and $M_t = 0.122$).

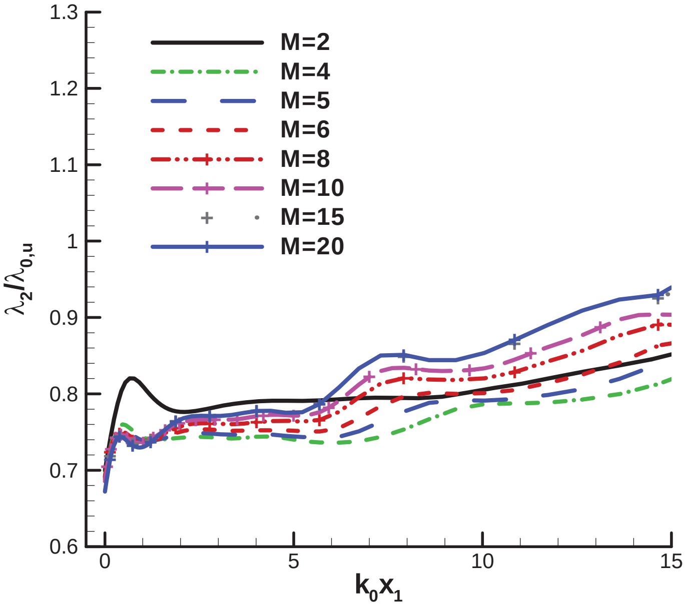

Fig. 35: Effect of increasing mean Mach number on transverse Taylor microscale for inflow of Case I ($\mathrm{Re}_\lambda = 6.2$ **and** $M_t = 0.121$ **).**

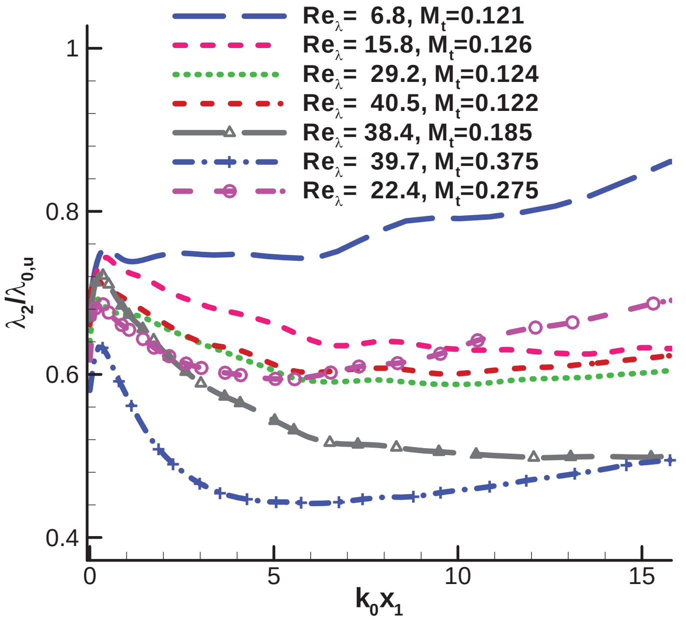

Fig. 36: Amplification of transverse Taylor microscale for seven different cases of inflow turbulence on interaction with a Mach 5 shock.

5.5.1 Effects of changing shock strength for fixed inflow turbulence.

Evolution of streamwise Taylor microscale, λ_1, from our shock fitting computation for varying shock strengths with inflow of Case III is presented in Fig. 32. Across the shock, the flow is compressed and streamwise Taylor microscale is reduced as predicted by LIA. Reduction in streamwise Taylor microscale across the shock remains between 80% to 85% for all the values of inflow mean Mach numbers considered. Downstream of the shock, λ_1 values increase rapidly. In the far-field, streamwise microscale is higher for stronger shocks.

The evolution of transverse Taylor microscales for the cases of Fig. 32 is shown in Fig. 33. The reduction in transverse Taylor microscale is around 35% across the shock wave for all the cases. The transverse scale then increases slightly within a distance of $\sim 0.5/k_0$ behind the shock. Further downstream, for weaker than Mach 10 shocks, we observe a decay in transverse Taylor microscale followed by a continuous increase. Smallest $\lambda_2/\lambda_{0,u}$ ratio is obtained for Mach 3 flows. For stronger than Mach 10 shocks, there is a monotonic increase in the Taylor miscroscale downstream of the shock.

The trends in the transverse microscales correspond very well to those noted for streamwise vorticity. Stretching and tilting of the fluid elements leads to increase in streamwise vorticity. The energy is transferred to small scales reducing the transverse Taylor microscale. These effects reverse for stronger than Mach 3 for the inflow of Case III. For a higher Reynolds number case, Case IV, the viscous effects are slightly weaker. As shown in Fig. 34, smallest $\lambda_2/\lambda_{0,u}$ ratio is now obtained for a Mach 4 shock. On the other hand, for the strongly viscous cases, Case I, this decay in Taylor microscale is not observed as shown in Fig. 35.

5.5.2 Effects of changing inflow conditions at fixed shock strength.

In this study, we compute seven different cases of inflow turbulence. Streamwise Taylor microscales (not shown here) has same value just behind the shock irrespective of inflow conditions and these values increase monotonically behind the shock for all cases. We present results for the transverse Taylor microscales after interaction of inflow with turbulence of these seven cases with a Mach 5 shock in Fig. 36. For these cases, we see a trend of decrease in transverse fluctuations as Reynolds number or turbulent Mach number is increased. Apart from cases with very viscous flows, transverse scale decrease and then increases behind the shock. Faster decay is observed for the flows of higher turbulent Mach number. These trends correspond very well to those observed for streamwise vorticity variations.

In literature, the practice is to compare the results of LIA against the far-field values. Such comparisons for some mean Mach numbers with inflow of the Case I are presented in our earlier work [10]. It should be noted, however, that unlike linear analysis, the far-field values are not constant for computed solutions. Hence, there is no logical point of reference for such comparisions. Therefore, detailed comparisions with LIA for all the inflow cases are not considered here.

6 SUMMARY AND CONCLUSIONS

Shock-fitting methods provide a promising, though rarely used, alternative for the computation of shock and turbulence interaction problems. In our previous studies, we have shown these methods to be superior to the commonly used shock-capturing methods for the problems where well defined shock is present. Utilizing the unique capabilities of the shock-fitting method, we carry out direct numerical simulation (DNS) of canonical shock-turbulence interaction while focusing on very strong shocks with mean Mach numbers of up to 20. Our results agree with those from linear theory and other numerical efforts for weaker than Mach 8 shocks. However, as we increase the shock strengths to the values beyond those considered in the past, new trends are observed. It was found that mean values of density and pressure in turbulent postshock flow is smaller than corresponding laminar values. The difference between turbulent and laminar postshock values decreases as shock strength is increased. For weaker than Mach 8 shocks root mean square values in shock deflections were found to vary linearly with turbulence intensity values ahead of the shock as predicted by linear theory. However, for stronger shocks, shock deflections are much higher than those predicted by the linear theory. Amplification in streamwise velocity fluctuations was observed to decrease for weaker than Mach 8 shocks. This is in accordance with the linear theory results. This trend, however, reverses for stronger shocks. Same trends were observed for turbulent kinetic energy. Vorticity fluctuations return to isotropy behind the shock. Our calculations show that, contrary to the previous findings for weaker shocks, increasing shock strength does not simply increase the streamwise vorticity fluctuations. In fact, beyond a certain Mach number, amplification in streamwise vorticity fluctuations decrease and return to isotropy is delayed. We observe that the shock-fitting method provides new trends in the flow regimes that were not considered in the past.

7 ACKNOWLEDGEMENTS

This research is supported by DOE Office of Science as part of a SciDAC (Scientific Discovery through Advanced Computing) project with "Science Application" in Turbulence and Dr. Lali Chatterjee as Program Manager. The authors would like to thank Dr. J. Larsson, Prof. S. K. Lele and Prof. P. Moin of the Stanford University; Drs. A. Cook, W. Cabot, B. Sjögreen of the Lawrence Livermore National Laboratory and Dr. H. C. Yee of the NASA Ames Research Center for their valuable suggestions during the course of this work. The results in this research were produced by TeraGrid resources provided by TACC Ranger and resources of the National Energy Research Scientific Computing Center.

8 REFERENCES

1. Lee, S., Lele, S. K., and Moin, P., *Interaction of isotropic turbulence with shock waves: effect of shock strength.* Journal of Fluid Mechanics, 1997. **340**: p. 225-247.
2. Mahesh, K.A., Lee, L., Lele, S. K., and Moin, P., *The interaction of an isotropic field of acoustic waves with a shock wave.* Journal of Fluid Mechanics, 1995. **300**: p. 383-407.
3. Mahesh, K.A., Lele, S. K., and Moin, P., *The influence of entropy fluctuations on the interaction of turbulence with a shock wave.* Journal of Fluid Mechanics, 1997. **334**: p. 353-379.
4. Jamme, S., Cazalbou, J. B., Torres, F., and Chassaing, P., *Direct numerical simulation of the interaction between a shock wave and various types of isotropic turbulence.* Flow, Turbulence and Combustion, 2002. **68**: p. 227-268.

5. Carpenter, M.H., and Casper, J. H., *Accuracy of shock capturing in two spatial dimensions.* AIAA Journal, 1999. **37**(9): p. 1072-1079.
6. Rawat, P.S., and Zhong, X. *High- Order Shock-Fitting and Front-Tracking Methods for Numerical Simulation of Shock- Disturbance Interactions*. in *AIAA paper 2009-1138*. 2009.
7. Rawat, P.S., and Zhong, X., *On High-Order Shock-Fitting and Front-Tracking Schemes for Numerical Simulation of Shock-Disturbance Interactions.* Journal of Computational Physics, 2010. **229**(19): p. 6744-6780.
8. Lee, T.K., and Zhong, X., *Spurious numerical oscillations in simulation of supersonic flows using shock-capturing schemes.* AIAA Journal, 1999. **37**(3): p. 313-319.
9. Rawat, P.S., and Zhong, X., *Numerical Simulations of Strong Shock and Disturbance Interactions Using High-Order Shock-Fitting Algorithms.* 2008. **AIAA paper 2008-0746**.
10. Rawat, P.S., and Zhong, X. *Numerical Simulation of Shock-Turbulence Interactions using High-Order Shock-Fitting Algorithms*. in *AIAA paper 2010-114*. 2010.
11. Kovasznay, L.S.G., *Turbulence in supersonic flow.* Journal of the Aeronautical Sciences, 1953. **20**(10): p. 657-682.
12. Ribner, H.S., *Convection of a pattern of vorticity through a shock wave.* NACA TN-2864 (Also as NACA Report 1164 1953), 1953.
13. Ribner, H.S., *Shock-turbulence interaction and the generation of noise.* NACA TN-3255 (Also as NACA Report 1233), 1954.
14. Ribner, H.S., *Acoustic energy flux from shock-turbulence interaction.* Journal of Fluid Mechanics, 1969. **35**: p. 299-310.
15. Moore, F.K., *Unsteady oblique interaction of a shock wave with a plane disturbances.* NACA TN-2879 (Also as NACA Rep. 1165), 1953.
16. McKenzie, J.F., and Westphal, K. O., *Interaction of linear waves with oblique shock waves.* Physics of Fluids, 1968. **11**: p. 2350-2362.
17. Goldstein, M.E., *Turbulence generated by the interaction of entropy fluctuations with non-uniform mean flows.* Journal of Fluid Mechanics, 1979. **93**: p. 209-224.
18. Lee, L., Lele, S. K., and Moin, P., *Direct numerical simulation of isotropic turbulence interacting with a weak shock wave.* Journal of Fluid Mechanics, 1993. **251**: p. 533-562.
19. Lee, L., Lele, S. K., and Moin, P., *Interaction of isotropic turbulence with a strong shock wave.* AIAA Paper 94-0311, 1994.
20. Mahesh, K.A., Moin, P., and Lele, S. K., *The interaction of a shock wave with a turbulent shear flow.* Report TF-69, Thermosciences Division, Mechanical Engineering Department, Stanford University, 1996.
21. Fabre, D., Jacquin, L., Garnier, E., and Sagaut, P. . *Linear interaction analysis: The effect of a shock wave on a homogeneous perturbation field and on an entropy spot*. in *High Speed Compressible Flows, Euromech 403*. 1999. Poitiers.
22. Fabre, D., Jacquin, L., and Sesterhenn, J., *Linear interaction of a cylindrical entropy spot with a shock.* Journal of Physics of Fluids A, 2001. **13**(8): p. 2403-2422.
23. Pao, S.P., and Salas, M. D., *A numerical study of two-dimensional shock vortex interaction.* AIAA Paper 81-1205, 1981.
24. Zang, T.A., Hussaini, M. Y., and Bushnell, D. M. , *Numerical Computations of Turbulence Amplification in Shock-Wave Interactions.* AIAA Journal, 1984. **22**(1): p. 13-21.

25. Hussaini, M.Y., Kopriva, D., Salas, M. D., and Zang, T. A., *Spectral methods for the Euler equations. II - Chebyshev methods and shock fitting.* AIAA Journal, 1987. **23**: p. 234-240.
26. Meadows, K.R., Kumar, A., and Hussaini, M. Y., *Computational Study on the Interaction between a vortex and a shock Wave.* AIAA Journal, 1991. **29**(2): p. 174-179.
27. Meadows, K.R., and Casper, J., *Computing unsteady shock waves for aeroacoustic applications.* AIAA Paper 1993-4329, 1993.
28. Grasso, F., and Pirozzoli, S. , *Shock-wave-vortex interactions: shock and vortex deformations, and sound production.* Theoretical and Computational Fluid Dynamics, 1993. **13**(6): p. 421-456.
29. Andreopoulos, Y., Agui, J. H., and Briassulis, G., *Shock wave-turbulence interactions.* Annual Review of Fluid Mechanics 2000. **32**: p. 309-345.
30. Lee, L., Moin, P., and Lele, S. K., *Interaction of isotropic turbulence with a shock wave.* Report TF-52. Dept. Mech. Eng., Stanford Univ., CA, 1992.
31. Hannappel, R., and Friedrich, R., *Direct numerical simulation of a Mach 2 shock interacting with isotropic turbulence.* Applied Scientific Research, 1995. **54**: p. 205-221.
32. Adams, N.A., and Shariff, K., *A high-resolution hybrid compact-ENO scheme for shock turbulence interaction problems.* Journal of Computational Physics, 1996. **127**(27): p. 57-.
33. Adams, N.A., and Shariff, K., *Direct numerical simulation of turbulent compression corner flow.* Theoretical and Computational Fluid Dynamics, 1998. **12**: p. 109-129.
34. Pirozzoli, S., *Conservative hybrid compact-WENO schemes for shock-turbulence interaction.* Journal of Computational Physics, 2002. **178**(1): p. 81-117.
35. Ducros, F., Ferrand, V., Nicoud, F.,Weber, C., Darracq, D., Gacherieu C., and Poinsot, T., *Large eddy simulation of the shock/turbulence interaction.* Journal of Computational Physics, 1999. **152**: p. 517-549.
36. Larsson, J., and Lele, S.K., *Direct numerical simulation of canonical shock/turbulence interaction.* Physics of Fluids, 2009. **21**(12): p. 126101-126101-12.
37. Grube, N.E., Taylor, E. M. and Martin, M. P., *Direct numerical simulation of shock-wave/isotropic turbulence interaction.* 2009. **AIAA paper 2009-4165**.
38. Sesterhenn, J., *Direct numerical simulation of the interaction of isotropic turbulence with a shock wave using shock-fitting.* Comptes rendus. Mecanique [1631-0721], 2005. **333**(1): p. 87-93.
39. Moretti, G., and Abbett, M. , *A time-dependent computational method for blunt body flows.* AIAA Journal, 1966. **4**: p. 2136-2141.
40. Moretti, G., and Bleich, G., *Three-dimensional flow around blunt bodies.* AIAA Journal, 1967. **5**: p. 1558-1562.
41. Moretti, G., *Three-dimensional supersonic flow computations.* AIAA Journal, 1963. **1**: p. 2192-2193.
42. Moretti, G., *Inviscid flowfield about a pointed cone at an angle of attack.* AIAA Journal, 1967. **5**: p. 789-791.
43. Neef T. D., a.M., G., *Shock fitting for everybody.* Computers and Fluids, 1980. **8**: p. 327-334.
44. Moretti, G., *The lambda-scheme.* Computers and Fluids, 1979. **7**: p. 191-205.
45. Moretti, G., and di Piano, M. T., *An improved lambda-scheme for one-dimensional flows.* NASA CR 3712, 1983. **15**.

46. Valorani, M., and Favini, B., *On the numerical integration of multidimensional initial boundary value problems for the Euler equations in quasi-linear form.* Numerical Methods for Partial Differential Equations, 1983. **14**: p. 781-814.
47. Zannetti, L., and Moretti, G., *Numerical experiments on the leading edge flow field.* AIAA Journal, 1982. **20**: p. 1668-1673.
48. Dadone, A., and Moretti, G., *Fast Euler solver for transonic airfoils.* AIAA Journal, 1988. **26**: p. 409-416.
49. Moretti, G., *A technique for integrating two-dimensional Euler equations.* Computers and Fluids, 1988. **15**: p. 59-75.
50. Moretti, G., *Experiments in multi-dimensional floating shock fitting.* Polytechnic Institute of Brooklyn, 1973. **PIBAL Rept 73-18, Aug 1973**.
51. Salas, M.D., *Shock-fitting method for complicated two-dimensional supersonic flows.* AIAA Journal, 1976. **14**(5): p. 583-588.
52. Moretti, G., *A technique for integrating two-dimensional Euler equations.* Computers and Fluids, 1987. **15**: p. 59-75.
53. Moretti, G., *Computations of flows with shock.* Annual Review of Fluid Mechanics, 1987. **19**: p. 313-337.
54. Moretti, G., *Thirty-six years of shock fitting* Computers and Fluids, 2002. **31**(4-7): p. 719-723.
55. Kopriva, D.A. *A multidomain spectral collocation computation of the sound generated by a shock-vortex interaction.* in *Computational Acoustics: Algorithms and Applications, 2, Eds. D. Lee and M.H. Schultz*. 1988. Amsterdam, Netherlands: Elsevier Science Publishers.
56. Kopriva, D.A., Zang, T., and Hussaini, M. Y., *Spectral methods for the Euler equations - the blunt body problem revisited* AIAA Journal, 1991. **29**(9): p. 1458-1462.
57. Kopriva, D.A., *Shock-fitted multidomain solution of supersonic flows.* Computer Methods in Applied Mechanics and Engineering, 1999. **175**(3-4): p. 383-394.
58. Cai, W., *High-order hybrid numerical simulations of two-dimensional detonation waves.* AIAA Journal, 1995. **34**(7): p. 1248-1255.
59. Zhong, X., *High-order finite-difference schemes for numerical simulation of hypersonic boundary-layer transition.* Journal of Computational Physics, 1998. **144**: p. 662-709.
60. Ma, Y., and Zhong, X., *Receptivity of a Supersonic Boundary Layer over a Flat Plate. Part 1: Wave Structures and Interactions.* Journal of Fluid Mechanics, 2003. **488**: p. 31-78.
61. Ma, Y., and Zhong, X., *Receptivity of a Supersonic Boundary Layer over a Flat plate. Part 2: Receptivity to Freestream Sound.* Journal of Fluid Mechanics, 2003. **488**: p. 79-121.
62. Ma, Y., and Zhong, X., *Receptivity to Freestream Disturbances of Mach 8 Flow over A Sharp Wedge*, in *41st AIAA Fluid Dynamics Conference and Exhibit*. 2003, AIAA paper 2003-0788.
63. Zhong, X., *Leading-Edge Receptivity to Free Stream Disturbance Waves for Hypersonic Flow over a Parabola.* Journal of Fluid Mechanics, 2001. **441**: p. 315-367.
64. Ma, Y., and Zhong, X., *Receptivity of a Supersonic Boundary Layer over a Flat Plate. Part 3: Effects of Different Types of Free-Stream Disturbances.* Journal of Fluid Mechanics, 2005. **532**: p. 63-109.

65. Brooks, G.P., and Powers, J. M., *Standardized pseudospectral formulation of the inviscid supsersonic blunt body problem.* Journal of Computational Physics, 2004. **197**(1): p. 58-85.
66. Moin, P., and Mahesh, K., *Direct Numerical Simulation: A tool in turbulence research.* Annual Review of Fluid Mechanics, 1998. **30**: p. 539-578.
67. Zhong, X., and Ma, Y., *Boundary-layer receptivity of Mach 7.99 Flow over a blunt cone to free-stream acoustic waves.* Journal of Fluid Mechanics, 2005. **556**: p. 55-103.
68. Taylor, G., I., *The spectrum of turbulence.* Proceedings of the Royal Society of London. Series A, Mathematical and Physical Sciences, 1938. **164**(919): p. 476-490.
69. Lee, L., Lele, S. K., and Moin, P., *Simulation of spatially evolving compressible turbulence and the applicability of Taylor's Hypothesis.* Physics of Fluids A, 1992. **4**: p. 1521-1530.
70. Erlebacher, G., Hussaini, Y., Kreiss, H. O., and Sarkar, S., *The Analysis and Simulation of Compressible Turbulence.* Theoretical and Computational Fluid Dynamics, 1990. **2**: p. 73-95.
71. Samtaney, R., Pullin, D. I., and Kosovic, B., *Direct numerical simulation of decaying compressible turbulence and shocklet statistics.* Physics of Fluids, 2001. **13**(5): p. 1415-1430.
72. Ristorcelli, J.R., and Blaisedell, G. A., *Consistent initial conditions for the DNS of compressible turbulence.* Physics of Fluids, 1997. **9**(1): p. 4-6.
73. Poinsot, T.J., and Lele, S. K., *Boundary conditions for direct simulations of compressible viscous flow.* Journal of Computational Physics, 1992. **101**(1): p. 104-129.
74. Lele, S.K., and Larsson, J., *Shock-turbulence interaction: What we know and what we can learn from peta-scale simulations.* Journal of Physics: Conference Series, 2009. **180**(012032).
75. Lele, S.K., *Shock-jump relations in a turbulent flow.* Physics of Fluids, 1992. **4**: p. 2900-2905.
76. Ribner, H.S., *Convection of a pattern of vorticity through a shock wave.* NACA TN-2864 (Also as NACA Report 1164), 1953.
77. Andreopoulos, Y., Agui, J. H., and Briassulis, G., *Shock wave-turbulence interactions.* Annual Review of Fluid Mechanics, 2000. **32**: p. 309-345.